STUDY OF ICE CLOUD PROPERTIES USING INFRARED SPECTRAL DATA

A Thesis

by

KEVIN JAMES GARRETT

Submitted to the Office of Graduate Studies of
Texas A&M University
in partial fulfillment of the requirements for the degree of

MASTER OF SCIENCE

August 2007

Major Subject: Atmospheric Sciences

STUDY OF ICE CLOUD PROPERTIES USING INFRARED SPECTRAL DATA

A Thesis

by

KEVIN JAMES GARRETT

Submitted to the Office of Graduate Studies of
Texas A&M University
in partial fulfillment of the requirements for the degree of

MASTER OF SCIENCE

Approved by:

Chair of Committee, Ping Yang
Committee Members, Shaima L. Nasiri
Gerald R. North
George Kattawar
Head of Department, Richard E. Orville

August 2007

Major Subject: Atmospheric Sciences

ABSTRACT

Study of Ice Cloud Properties Using Infrared Spectral Data. (August 2007)

Kevin James Garrett, B.S., Syracuse University

Chair of Advisory Committee: Dr. Ping Yang

The research presented in this thesis involves the study of ice cloud microphysical and optical properties using both hyperspectral and narrowband infrared spectral data. First, ice cloud models are developed for the Infrared Atmospheric Sounding Interferometer (IASI) instrument onboard the METOP-A satellite, which provide the bulk-scattering properties of these clouds for the 8461 IASI channels between 645 and 2760 cm^{-1}. We investigate the sensitivity of simulated brightness temperatures in this spectral region to the bulk-scattering properties of ice clouds containing individual ice crystal habits as well as for one habit distribution. The second part of this thesis describes an algorithm developed to analyze the sensitivity of simulated brightness temperatures at 8.5 and 11.0 μm to changes in effective cloud temperature by adjusting cloud top height and geometric thickness in a standard tropical atmosphere. Applicability of using these channels in a bi-spectral approach to retrieve cirrus cloud effective particle size and optical thickness is assessed. Finally, the algorithm is applied to the retrieval of these ice cloud properties for a case of single-layered cirrus cloud over a tropical ocean surface using measurements from the Moderate Resolution Infrared

Spectroradiometer (MODIS). Cloud top height and geometric thickness in the profile are adjusted to assess the influence of effective cloud temperature on the retrieval.

DEDICATION

To all of my friends and family who have given me so much encouragement to pursue a career in a field that I love, and to those that have supported me during this 3-year venture.

ACKNOWLEDGEMENTS

I would like to thank my advisor, Dr. Ping Yang, for providing me the opportunity to become involved in such an exciting and rapidly advancing field, for his support, motivation, guidance and passion for mentoring myself as well as the entire research group. I would also like to extend deepest gratitude to the rest of my thesis committee, particularly Dr. Shaima Nasiri for her support, encouragement and technical guidance, Dr. Gerald North for his advice and encouragement prior to my applying as a post-baccalaureate and throughout, and Dr. George Kattawar. Also, I would like to acknowledge and thank Dr. Don Collins as chair of the graduate admissions committee for providing me with guidance during my post-baccalaureate semester and for giving me the valuable opportunity as a teaching assistant during my first year as a graduate student, and the rest of the faculty at Texas A&M University from whom I have learned so much.

I also would like to thank my fellow research group members, especially Zhibo Zhang, Dr. Gang Hong and Kerry Meyer for all of their help, support, and hours of valuable discussion. Thanks to Chris Yost, for being such a great friend, as well as for providing me with code. Also I thank Bryan Baum for his assistance with the correlated *k*-distribution routines, ice crystal models and discussions at conferences.

Lastly I would like to thank all of my family and friends for their encouragement, especially Katie Collins who has been so supportive.

This study is partly supported by the National Science Foundation Physical Meteorology Program managed by Dr. Andrew Detweiler (ATM-0239605), and by a NASA research grant (NNG04GL24G) from the Radiation Sciences Program managed by Dr. Hal Maring and NASA MODIS program managed by Dr. Paula Bontempi.

TABLE OF CONTENTS

Page

ABSTRACT iii

DEDICATION v

ACKNOWLEDGEMENTS vi

TABLE OF CONTENTS viii

LIST OF FIGURES x

LIST OF TABLES xiii

1. INTRODUCTION 1

2. ICE CLOUD MODELS 7

2.1 Methodology 7
2.2 The Infrared Atmospheric Sounding Interferometer 8
2.3 Single-Scattering Properties Database 9
2.4 Bulk-Scattering Properties Computation 20
2.5 IASI Spectral Simulations 31

3. SENSITIVITY OF INFRARED BRIGHTNESS TEMPERATURES TO CLOUD TEMPERATURE 40

3.1 Methodology 41
3.2 Sensitivity to Cloud Top Temperature 43
3.3 Sensitivity to Cloud Layer Temperature 46

Page

4. INFLUENCE OF CLOUD TEMPERATURE ON THE RETRIEVAL OF CIRRUS PROPERTIES 52

4.1 Methodology 52
4.2 Instruments and Data 53
4.3 Retrievals with Varying Cloud Top Height 55
4.4 Retrievals with Varying Geometric Thickness..... 63

5. DISCUSSION AND SUMMARY 70

REFERENCES..... 73

VITA……...……..82

LIST OF FIGURES

FIGURE Page

1 Images of the 6 non-spherical ice crystal habits included in the single-scattering property database of Yang *et al.* [56]...10

2 The refractive index of ice over the IASI spectrum for a) real part and b) imaginary part...14

3 Interpolated single-scattering properties as a function of wavelength for 6 ice crystal habits...15

4 Interpolated single-scattering properties as a function of maximum dimension for 6 ice crystal habits...16

5 Interpolated scattering phase functions of 6 ice crystal habits...18

6 Comparison of interpolated (line) and original (+) single-scattering databases for aggregates with D_{max} of 30 and 50 μm at a wavelength of 11.2 μm...19

7 Bulk single-scattering phase functions for 6 individual ice crystal habits compared with the Baum v2 for a D_e of 30 μm...26

8 Bulk-scattering properties for 6 individual ice crystal habits compared with properties from Baum v2 habit distribution with an effective size of 30 μm as a function of wavelength...28

9 Bulk-scattering properties for 6 individual ice crystal habits compared with properties from Baum v2 habit distribution with an effective size of 50 μm as a function of wavelength...29

10 Bulk-scattering properties for 6 individual ice crystal habits compared with properties from Baum v2 habit distribution with an effective size of 100 μm as a function of wavelength...30

11 Simulated brightness temperatures of clouds with an effective diameter of 30 μm for optical thickness of 0.1 (black), 1.0 (red), 2.0 (green), and 5.0 (blue)...35

FIGURE Page

12 Simulated brightness temperatures of clouds with the habit distribution of Baum *et al*. [4] for clouds with effective diameters of 30, 50 and 100 μm and optical thicknesses of 0.1, 1.0, 2.0, and 5.0..…..…..…..……..37

13 Difference of the simulated brightness temperatures of clouds using the Baum *et al.* [4] habit distribution and individual ice crystals …….……...39

14 Simulated brightness temperatures at 8.5 and 11.0 μm as a function of optical thickness, for clouds of varying height…….……..45

15 Simulated 8.5 and 11.0 μm BTs for clouds with varying geometric thicknesses of 1, 2, 3, and 5 km minus BTs of a cloud with a fixed geometric thickness of 0.5 km as a function of optical thickness.……..…..…48

16 Simulated 8.5 and 11.0 μm BTs for clouds with varying geometric thicknesses of 1, 2, 3, and 5 km minus BTs of a cloud with a fixed geometric thickness of 0.5 km as a function of optical thickness.…..…....…..51

17 False color image of MODIS case area from granule MYD021KM.A2005354.0140, approximately ~1100 pixels.…….……...56

18 a) MODIS retrieved cloud optical thickness, b) MODIS retrieved effective radius and c) collocated AIRS pixels within the scene…..…..…….…….56

19 IR bi-spectral plots for clouds with varying height…….....…….……...58

20 Geolocated retrieved optical thickness and effective radius of case area for varying cloud height……...……...…….…….……...60

21 Scatter plots comparing retrieved values of optical thickness and effective radius to MODIS MOD06 retrieved values corresponding to the plots in Fig. 20……..…….……..61

22 IR bi-spectral plots for a cloud at the AIRS derived cloud top pressure level with varying geometric thickness…….…….…….65

23 Geolocated retrieved optical thickness and effective radius of case area for a cloud at the AIRS derived cloud top pressure level and varying geometric thickness…….……...…...67

FIGURE Page

24 Scatter plots comparing retrieved values of optical thickness and effective radius to MODIS MOD06 retrieved values corresponding to the plots in Fig. 23..……...……..……...……..68

LIST OF TABLES

TABLE Page

1 Habit distribution from Baum *et al* [4] listing the percentage of each habit with given maximum dimension……..…..……...…..…...24

2 Cloud and profile data for three retrievals with varied cloud top height……....59

3 Cloud and profile data for three retrievals with varied cloud geometric thickness…….…….……64

1. INTRODUCTION

Studies have shown that cirrus clouds occur roughly 30 – 40% of the time globally [52], with higher frequencies in the tropics [9]. With their frequent occurrence, cirrus clouds have a large impact on the Earth's radiation budget by reflecting incoming solar radiation (albedo effect) and trapping terrestrial thermal emission (greenhouse effect). Cirrus clouds here are defined as any cloud composed of only ice crystals, including the upper anvil regions of deep convection. The amount of solar radiation reflected by a cirrus cloud is mainly a function of its microphysical properties, such as ice crystal size, habit (shape), and ice-water content (IWC). The amount of thermal radiation transmitted through and emitted by a cirrus cloud also depends on microphysical properties, but is also strongly dependent on surface and cloud temperatures. The relative strengths of these processes determine the net cloud radiative forcing, or whether cirrus clouds have a warming or cooling effect on climate.

In order to describe and predict how cirrus clouds affect climate, we must have the ability to characterize cirrus clouds accurately in climate models. Discrepancies in calculated cloud radiative forcing among climate models exist and are largely due to the uncertainties associated with cirrus clouds and how they are characterized [37], [47]. To increase confidence in climate model results, a global, diurnal cirrus cloud climatology on high-resolution time and spatial scales is necessary. Satellite remote sensing may be

---

This thesis follows the style of *IEEE Transactions on Geoscience and Remote Sensing*.

the most effective tool to observe cirrus clouds and retrieve properties such as effective particle size, cloud optical thickness, height, and geometric thickness, which are important in climate studies and necessary to construct this climatology [50].

Since the intensity and direction of reflected solar radiation from cirrus clouds largely depends on ice crystal size and shape, underlying surface albedo [29], [49], and the direction of the incident radiation, the inference of cirrus properties can be made from top-of-atmosphere satellite observations of the reflectance at certain wavelengths. For daytime retrievals of cirrus properties, the only other required information is the cirrus cloud bulk-scattering properties, which depend on assumptions made about the particle size and habit distributions within the cloud. The scattering properties and viewing geometries may then be used to simulate the reflectance of model cirrus clouds with various effective sizes and optical thicknesses in order to infer these properties from the observed reflectance of any cirrus cloud.

Methods of estimating cirrus cloud properties using reflected solar radiation are well established. Principal retrieval schemes are based on bi-directional reflectance at two bands in the visible and near-infrared (NIR) spectrums, with one band sensitive to effective size and the other sensitive to optical thickness. More prominent retrievals use the measured reflectance at 2.13-μm, which is sensitive to effective size, and the 0.66-μm (or 0.85-μm over ocean surfaces) that is essentially a function of optical thickness [31], [33]. In fact, this approach is currently applied to the Moderate Resolution Imaging Spectroradiometer (MODIS) operational cloud product, MOD06 [36]. The method works best for optically thicker cirrus ($\tau_{0.55} > 1$), since cirrus clouds that exhibit

low reflectance values ($R_{2.13}$, $R_{0.66} < 0.1$) in each channel have decreased sensitivity to particle size and increased interdependence between particle size and optical thickness.

Utilizing techniques to derive reflectance at 0.66 and 1.38 μm [18], Meyer *et al.* [27] developed a method to retrieve optical thickness from more tenuous cirrus clouds using MODIS observed radiances at these wavelengths. Unlike visible and near-infrared (NIR) window channels, the 1.38 μm channel is located in a strong water vapor absorption band. Reflected radiation at this channel is mainly sensitive to high cirrus clouds, and is not usually contaminated by surface or low-level water clouds because lower-tropospheric water vapor absorbs the radiation. This approach illustrates the desire to minimize the noise contributed from the background atmospheric state, allowing simplification of the model and increasing confidence in the result.

During nighttime, top-of-atmosphere (TOA) observations of cirrus clouds are made with measurements at infrared (IR) wavelengths sensitive to the retrieved properties. However, the measured intensity of the upwelling radiation not only depends on the bulk-scattering properties of ice crystals, as with daytime solar reflectance, but also on a variety of atmospheric and surface parameters. In most techniques, relevant ice cloud models, along with accurate knowledge about the atmospheric temperature and moisture profile, skin temperature, surface albedo, cloud top height, and cloud geometric thickness, are required to attain confidence in retrievals of cirrus cloud microphysical and optical properties. Error in the assumptions made about these parameters will lead to errors in the inferred cirrus cloud properties [24]. The uncertainty in these

assumptions has led to the development of several IR-based retrievals of cirrus cloud properties using both narrowband and hyperspectral measurements.

Static lookup libraries that link effective size and optical thickness to simulated visible and NIR reflectance values for a range of viewing geometries are the strength of many daytime cirrus retrievals. In IR-based retrievals, the variability of the environment in which cirrus may be located may have as much influence on the observed IR radiance as the cirrus cloud itself (especially for optically thin cirrus), requiring a lookup library which contains every possible combination of atmospheric profile, cloud top height and geometric thickness. When applied to a global retrieval of cirrus properties, this approach becomes computationally expensive and impractical. However, radiometric measurements from several hyperspectral and narrowband infrared sensors have been used to perform retrievals of cirrus cloud properties with sensitivity analyses for varying atmospheric and surface parameters.

The spectral region between 750-1000 cm^{-1} has been studied extensively for sensitivity to cirrus cloud effective size [3]. Wei *et al.* [48] showed that the slope of brightness temperatures (BTs) within this region through Atmospheric Infrared Sounder (AIRS) observations, along with data from the 1070-1135 cm^{-1} band, could be used to retrieve ice cloud optical thickness for clouds with visible optical thickness less than 10. Similarly, Huang *et al.* [24] used these spectral regions to simultaneously retrieve effective size and optical thickness from high-resolution interferometer sounder (HIS) data collected during the FIRE-ACE field campaign. Error of about 10-15% in these retrievals was demonstrated due to error in assumed cloud temperature (height) for

optically thick cloud, and surface skin temperature for optically thin cloud. However, for clouds with optical thickness greater than 5, BTs become constant across the spectral region causing difficulty for retrieval of cirrus cloud properties.

Other studies have included narrowband IR measurements. Chiraico *et al.* [10] used MODIS split-window observation at 8.65, 11.15 and 12.05 μm to retrieve the effective size of ice crystals, and reduced uncertainty in the retrievals with depolarized lidar measurements by 20-65%. Baum *et al.* [5] used theoretical calculations at 8 and 11.0 μm to infer effective size and optical thickness from MODIS Airborne Simulator (MAS) data, with consistency in optical thickness but discrepancy among effective size when compared to solar and NIR-based retrievals.

Studies have also explored approaches that may be independent of the sensitivity of IR observations to assumptions sometimes required by cirrus retrieval models. Emissivities at 8.3 and 11.1 μm from the TIROS-N Operational Vertical Sounder have been used to retrieve effective size, independent of atmospheric state and with little sensitivity to cloud height or geometric thickness [39], [43]. Nasiri *et al.* [34] demonstrated that the difference between simulated 8.5 and 11.0 μm brightness temperatures ($BTD_{8.5\text{-}11.0}$) exhibited little sensitivity to certain assumptions regarding the particle size and habit distributions used to compute the bulk-scattering properties.

Even with the wide range of methodologies employed for IR-based retrievals, the sensitivities to variable atmospheric parameters are still not fully understood to the point where simplifications in models can be made to achieve practical or operational use. Because of the uncertainty with nighttime retrieval results, the diurnal climatology

required to compare with climate model output remains incomplete. In this thesis, we will investigate application of both hyperspectral and narrowband remote sensing using IR spectral data to the retrieval of cirrus cloud microphysical properties, with specific focus on the influence of ice cloud model and cloud temperature assumptions.

In Section 2, we detail the development of ice cloud models that provide bulk-scattering properties of ice crystals, such as extinction efficiencies, single-scattering albedo, and scattering phase functions. The ice cloud models will be developed for the Infrared Atmospheric Sounding Interferometer (IASI) onboard the METOP-A satellite. Simulations of the hyperspectral domain covered by IASI are performed for various clouds to illustrate how the ice cloud models may be used to retrieve effective size and optical thickness with IASI data. Simulations using different ice cloud models are performed to demonstrate the influence of assumed ice crystal habits on top-of-atmosphere BTs. In Section 3, a model is developed to investigate the influence of cloud temperature on simulated 8.5 and 11.0 μm BTs at top-of-atmosphere due to changes in cloud top height and geometric thickness, for a variety of single-layer, tropical cirrus clouds. We examine the results for the types of clouds of which the model is most sensitive to. In Section 4, the model is applied to a retrieval of cirrus cloud effective size and optical thickness using MODIS observed radiances at 8.5 and 11.0 μm. Cloud top height and geometric thickness are adjusted based on Atmospheric Infrared Sounder (AIRS) data, and results for each case are compared to assess the influence of cloud temperature on the IR-based retrievals using the $BTD_{8.5\text{-}11.0}$ bi-spectral approach.

2. ICE CLOUD MODELS

The retrieval of cirrus cloud optical and microphysical properties requires some assumptions about surface, atmospheric and cloud single-scattering properties. Many retrieval methods simulate brightness temperatures over a range of cirrus clouds using a radiative transfer model (RTM), which can then be matched to satellite observations for inference of cloud properties. Since most clouds are assumed to be composed of ice crystals of various habits (shapes) and sizes, the cirrus cloud in the RTM is defined by bulk-scattering properties such as the extinction efficiency and single-scattering albedo. The bulk-scattering properties are computed based on a variety of observed ice crystal particle size distributions and assumed habit distributions, and are the basis of the ice cloud model. However, ice cloud models are not universal; they depend on the characteristics of the observing satellite instrument, such as the spectral response function, and on the radiative transfer model used to simulate radiation above a cirrus cloud.

2.1 Methodology

In this section, we detail the development of ice cloud models for use with the Infrared Atmospheric Sounding Interferometer (IASI). The models are constructed based on a single-scattering properties database developed by Yang *et al.* [56]. This database contains the single-scattering properties for 6 ice crystal habits from visible to

far IR wavelengths. To match the spectral coverage of the IASI instrument, the database is interpolated from 28 to 8461 IR wavelengths. The bulk-scattering properties are then computed for each of the 6 ice crystal habits, as well as for 1 habit distribution following methods and using data from Baum *et al.* [7]. Finally, simulations of the IASI spectrum are performed for a variety of cloud configurations to compare the sensitivities of TOA brightness temperatures to the differences in the ice cloud models.

2.2 The Infrared Atmospheric Sounding Interferometer

On October 19, 2006, the European Organisation for the Exploitation of Meteorological Satellites (EUMETSAT) in conjunction with the French space agency CNES, successfully launched the Meteorological Operational satellite METOP-A. METOP-A is a sun-synchronous polar-orbiting satellite with an altitude of 817 km and crosses the equator at 9:30 local time, achieving global coverage in 12 hours.

Onboard the METOP-A satellite is the Infrared Atmospheric Sounding Interferometer (IASI). IASI is a Michelson interferometer with continuous spectral coverage between 645 and 2760 cm^{-1} (3.62 – 15.5 μm) at a resolution of 0.25 cm^{-1} equaling 8461 channels [38]. The instrument was primarily developed to improve medium-range weather forecasting by providing atmospheric temperature soundings within an accuracy of 1 K per 1 km and humidity soundings to within 10% over an instantaneous field-of-view (IFOV) of 25 km at nadir. While the instrument was developed for atmospheric sounding, the spectral coverage and resolution invite the retrieval of ice cloud optical and microphysical properties. The first step in developing a

retrieval method for IASI is the development of ice cloud models which include computing the bulk-scattering properties necessary for RTM simulations. The ice cloud models may also prove useful in current operational algorithms for IASI, such as cloud clearing which is necessary to perform sounding in a cloudy field-of-view.

2.3 Single-Scattering Properties Database

To develop the ice cloud models, the single-scattering properties for individual ice crystal habits must first be computed for a range of size bins given by ice crystal maximum dimension. Earlier methods to compute these properties employed Mie theory [51] and ray tracing techniques [44], but these approaches limit application in remote sensing to spherical and hexagonal ice crystals [11], [28]. With the implementation of the Finite Difference Time Domain (FDTD) [54] and the Improved Geometric Optics Method (IGOM) [55] to light scattering of ice crystals, a library of single-scattering properties was constructed for a larger variety of pristine and complex ice crystal surrogates [57].

The most recent database from Yang *et al.* [56] includes the single-scattering properties for 8 ice crystal habits (Fig. 1): aggregates, droxtals, plates, solid columns, hollow columns, 6-branch bullet rosettes, spheres and spheroids. The inclusion of the droxtal shape is meant to represent small, nearly spherical ice crystals found near the tops of cirrus clouds, thus the single-scattering properties for spheres and spheroids are

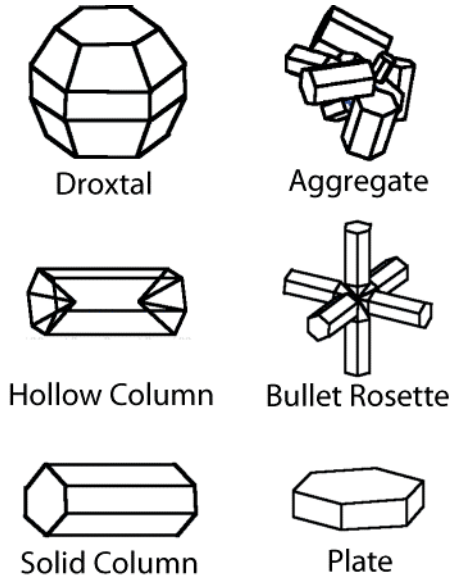

Fig. 1. Images of the 6 non-spherical ice crystal habits included in the single-scattering property database of Yang *et al.* [56].

not used in the ice cloud models [53]. The properties calculated include the scattering phase function, which describes the angular distribution of radiation scattered by a particle. The phase function, computed for 498 scattering angles between 0 º and 180º can be defined as

$$P(\cos\theta) = \sum_{\ell=0}^{N} \varpi_\ell P_\ell(\cos\theta), \tag{1}$$

where P_ℓ is the ℓ^{th} order Legendre polynomial, θ is the scattering angle, and ϖ_ℓ is the expansion coefficient equal to

$$\varpi_\ell = \frac{2\ell+1}{2}\int_{-1}^{1} P(\cos\theta)P_\ell(\cos\theta)d(\cos\theta). \tag{2}$$

For the first moment of the phase function $\ell = 1$, the equation defines the asymmetry factor, or cosine weighted average value of the phase function,

$$g = \frac{\varpi_1}{3} = \frac{1}{2}\int_{-1}^{1} P(\cos\theta)\cos\theta d\cos\theta. \tag{3}$$

The asymmetry factor may range from $-1 \le g \le 1$ where $g = -1$ defines totally backscattered radiation, $g = 1$ defines radiation scattering only in the forward direction, and $g = 0$ when radiation is scattered isotropically, such as Rayleigh scattering.

The database also includes other properties important for radiative transfer calculations such as the extinction efficiency, Q_e, the scattering, absorption and extinction cross sections, σ_s, σ_a, and σ_e, respectively, as well as the single-scattering albedo defined as

$$\omega = \frac{\sigma_s}{\sigma_e}, \tag{4}$$

which is equal to 1 if no radiation is absorbed by the scattering particle.

The ice crystal habits are discretized into 45 size bins, with bin center maximum dimensions ranging from 2.0 – 9500 μm. The single-scattering properties are calculated at 65 visible and IR wavelengths from 0.2 – 100 μm. For size parameters $x = \pi D/\lambda$ less than 20, where D is the ice crystal maximum dimension and λ is the incident wavelength, the FDTD method is used to compute the single-scattering properties [54]. For size parameters greater than 20, this method becomes exceedingly computationally expensive. For moderate to large size parameters, the most current techniques to compute the single-scattering properties of ice crystal include the T-matrix method, Lorentz-Mie theory, and IGOM. However, between size parameters of 20 and 1000, the solutions of each method differ. To compute the single-scattering properties for size parameters larger than 20, Fu *et al.* [16], [17] developed the composite method. This method uses a combination of the Lorentz-Mie theory solution of spherical equivalent particles, the IGOM solution and the FDTD solution to compute each single-scattering property. For example, the absorption coefficient, Q_a, may be computed by

$$Q_a(L) = \begin{cases} Q_{aFDTD}(L) & (L < 20\lambda/\pi) \\ C_1 Q_{aMie}(L) + C_2 Q_{aIGOM}(L) & (L \geq 20\lambda/\pi) \end{cases}, \tag{5}$$

where $Q_{aFDTD}(L)$ is the absorption coefficient solution from the FDTD method for size parameters < 20, and $Q_{aMie}(L)$ and $Q_{aIGOM}(L)$ are the absorption coefficients from Lorentz-Mie and IGOM for size parameters ≥ 20, respectively. To ensure a smooth transition in size parameter domain for the single-scattering solutions from FDTD to the composite method, the coefficients C_1 and C_2 are determined by

$$Q_{aFDTD}(L_c) = C_1 Q_{aMie}(L_c) + C_2 Q_{aIGOM}(L_c), \tag{6}$$

where L_c is the largest maximum dimension derived from the FDTD method.

To match the spectral resolution of the database with that of IASI, the single-scattering properties must be interpolated. We select 28 wavelengths from 3.5 – 16.2 μm in the database and interpolate the single-scattering properties to 8461 wavelengths between 3.62 and 15.5 μm (645 – 2760 cm^{-1}). The properties, Q_e, ω, and g, can be interpolated linearly. However, the scattering phase function, $P(\cos\theta)$, must be interpolated using cubic spline interpolation. After interpolation, $P(\cos\theta)$ is renormalized.

The single-scattering properties for each individual ice crystal depend strongly on its size and shape, and also on the index of refraction of ice which varies with wavelength. Fig. 2 shows the refractive index of ice for both the real and imaginary parts, over the IASI spectral region. These indices show that the scattering and absorption properties of ice crystals vary significantly across the spectrum. Computed single-scattering properties must therefore demonstrate scattering and absorption features closely following the index of refraction of ice, in order for the ice cloud models to be of relevance to cirrus cloud property retrievals which depend on these scattering and absorption differences.

Fig. 3 shows the interpolated extinction efficiency, single-scattering albedo, and asymmetry factor as a function of wavelength across the entire IASI spectrum, for maximum dimensions of 10 and 50 μm. Although the properties vary similarly across

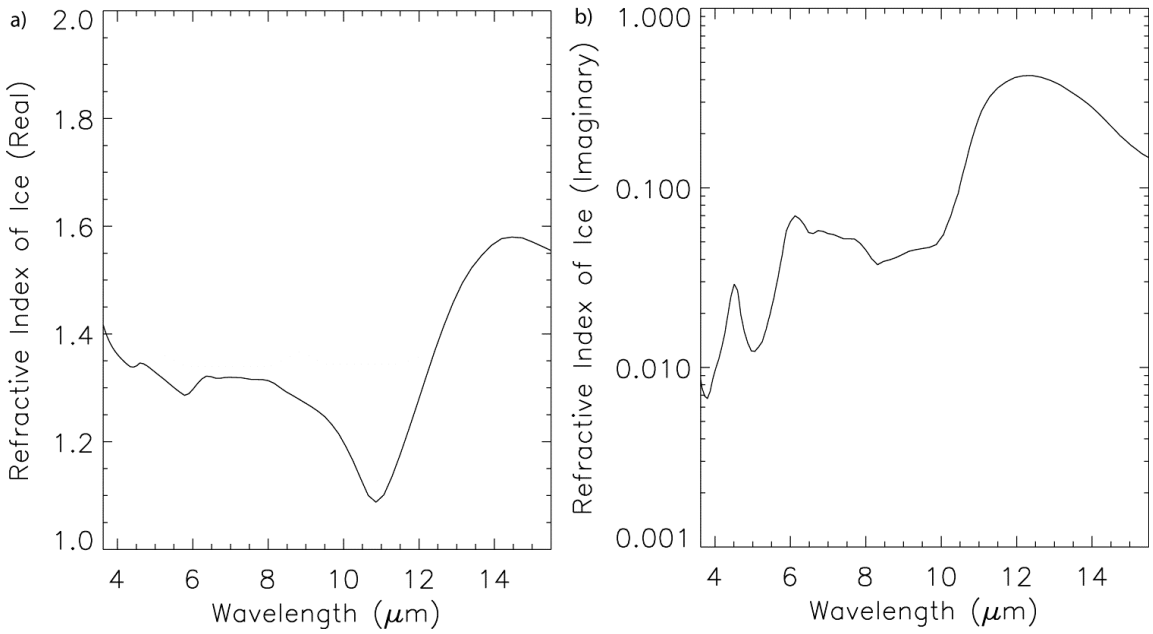

Fig. 2. The refractive index of ice over the IASI spectrum for a) real part and b) imaginary part. Data is taken from Warren [46].

the spectrum for each ice crystal habit, following the imaginary part of the index of refraction of ice closely (Fig. 2b), the magnitude of the properties vary significantly between the habits due to differences in their shape. For 10 μm ice crystals, the differences are more pronounced. However for 50 μm ice crystals, differences between the properties of the habits decrease as the size parameter increases, again due to absorption being the primary feature for large ice crystals at IR wavelengths. Again the absorption feature around 11.0 μm is noticeable. In Fig. 3e, the asymmetry factor for 10 μm sized ice crystals decreases monotonically across the spectrum, as absorption increases with increasing wavelength. However for larger sized crystals, as in Fig. 3f, diffraction dominates and the asymmetry factor is very close to 1 across the spectrum.

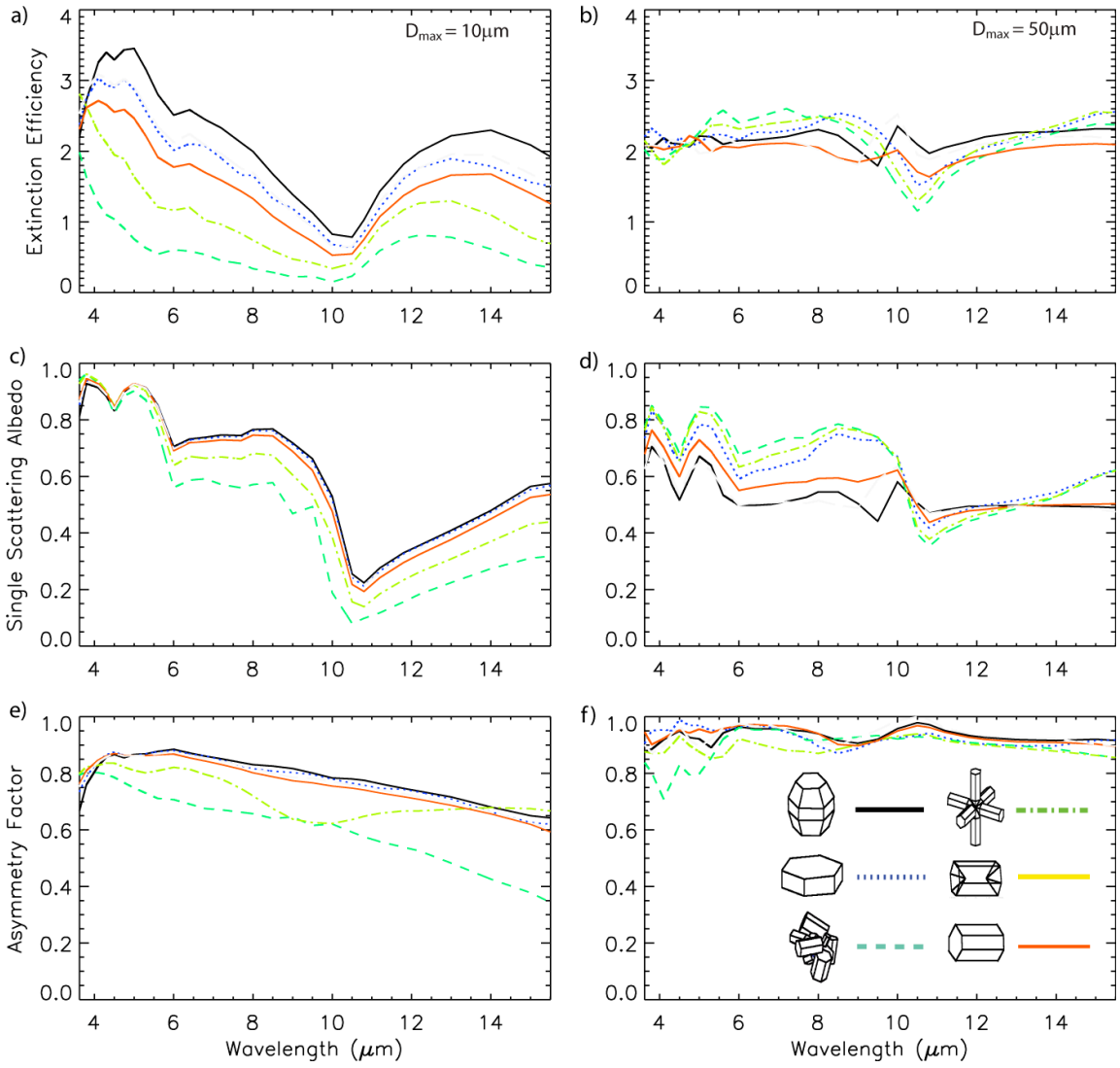

Fig. 3. Interpolated single-scattering properties as a function of wavelength for 6 ice crystal habits. Shown are a), b) the extinction efficiency for D_{max} of 10 and 50 μm respectively, c), d) the single-scattering albedo for D_{max} of 10 and 50 μm, respectively, and e), f) the asymmetry factor for D_{max} of 10 and 50 μm, respectively.

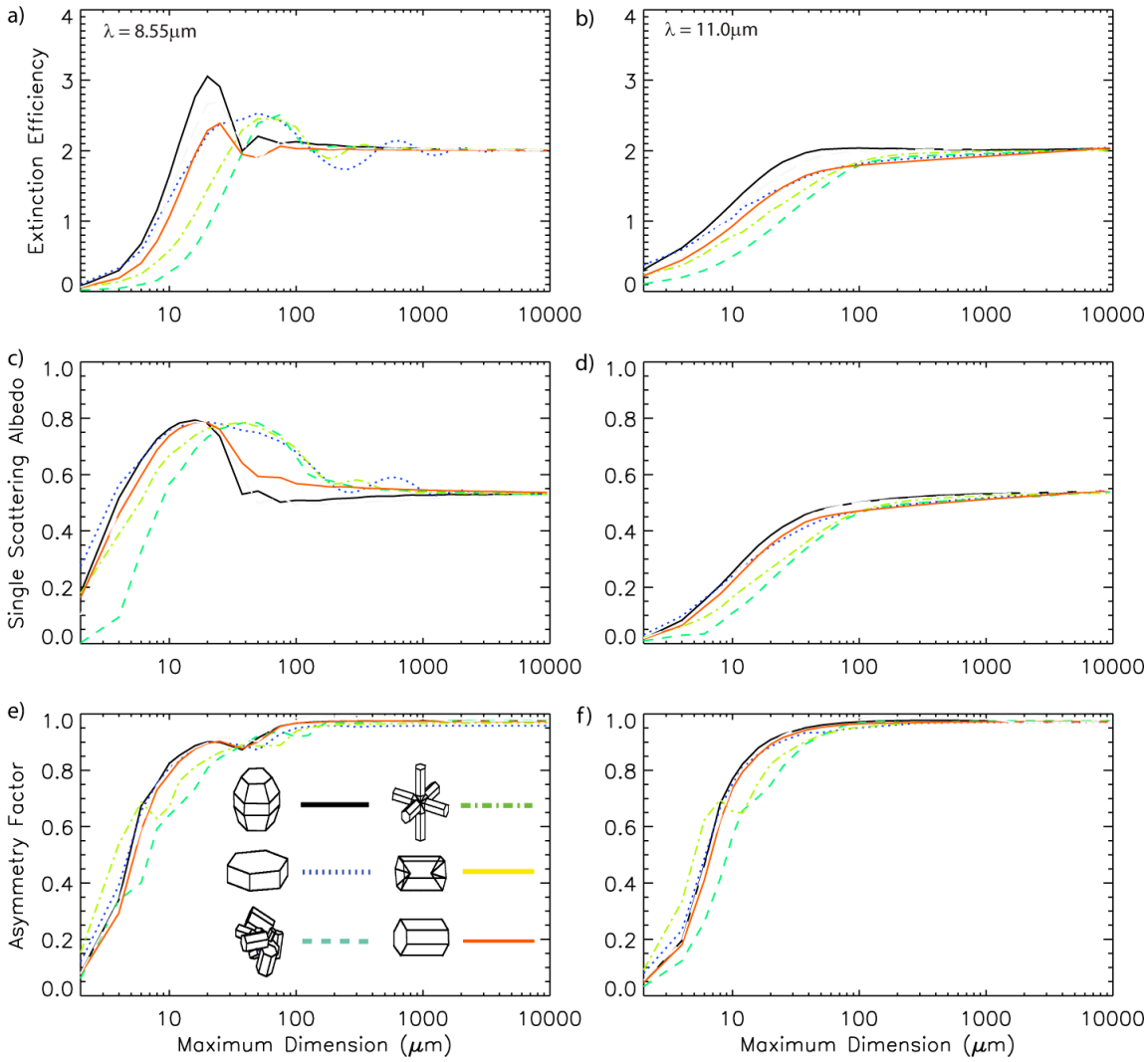

Fig. 4. Interpolated single-scattering properties as a function of maximum dimension for 6 ice crystal habits. Shown are a), b) The extinction efficiency at 8.55 and 11.0 μm, respectively, c), d) the single-scattering albedo at 8.55 and 11.0 μm respectively, and e), f) the asymmetry factor at 8.55 and 11.0 μm.

Fig. 4 illustrates the interpolated single-scattering properties for each of the 6 ice crystal habits as a function of maximum dimension for wavelengths of 8.55 and 11.0 μm. Oscillations in the 8.55 μm extinction efficiency occur for all habits with D_{max} between 20 and 500 (small size parameters). These are due to phase interference caused by the competing processes of diffraction and reflection/refraction [30]. As an incident light beam interacts with the ice crystal, some energy is diffracted by the particle but its phase remains constant. However, localized rays also enter the ice crystal where they may undergo a phase lag from internal reflection and refraction before exiting out of the particle. Light may also enter the particle from the diffracted portion in a process called tunneling, and this contributes to absorption, internal reflection and refraction [35]. Peaks in the extinction efficiency occur when energy from the processes are mapped to the far electric field and are in phase, also called the resonance region. Minima occur when the energy from the processes are completely out of phase. The amplitude of the oscillations, maxima, and minima are a function of index of refraction, wavelength, and ice crystal habit. Values of extinction efficiency converge to 2 as particle size increases because of increased absorption. The same pattern is recognized in the plot of single-scattering albedo (Fig. 4c), with the value converging to around 0.56 where absorption dominates in larger particles. In Fig. 4e, the asymmetry factor converges very near to 1 as diffraction dominates reflection and refraction for larger particles, and there is almost no backscattering. The same oscillation pattern is not apparent in the 11.0 μm plots, as ice absorption at this wavelength is a lot stronger (Fig. 2b).

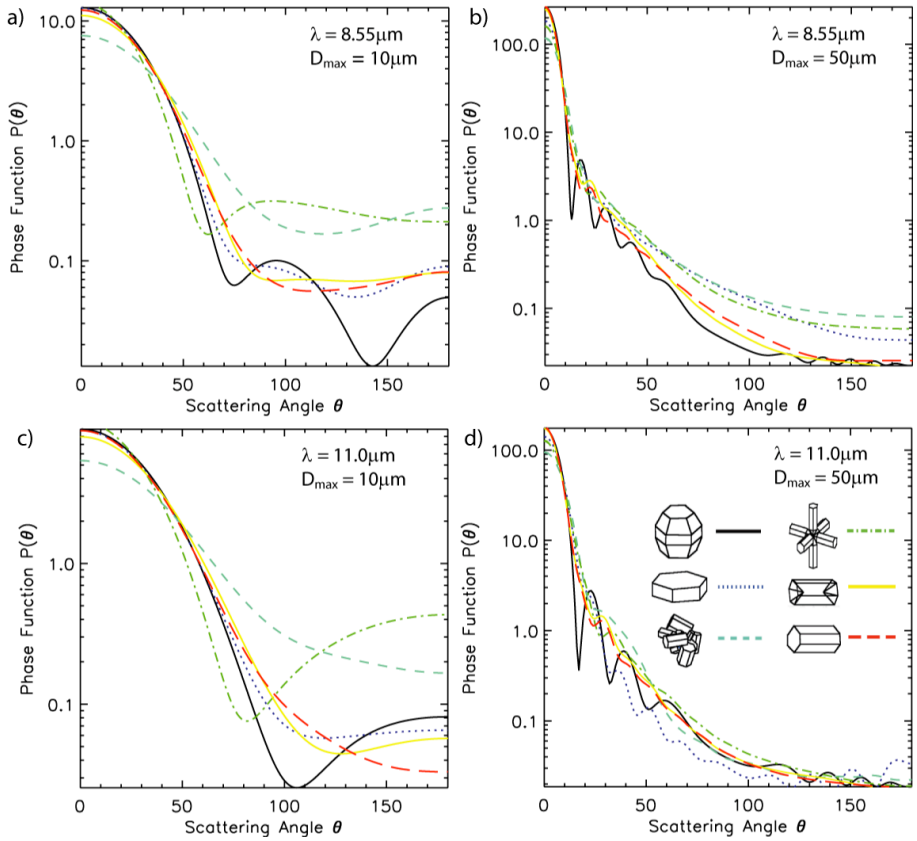

Fig. 5. Interpolated scattering phase functions of 6 ice crystal habits. Phase functions are plotted for wavelengths and maximum dimensions of a) λ = 8.55 μm and D_{max} = 10 μm, b) λ = 8.55μm and D_{max} = 50 μm, c) λ = 11.0 μm and D_{max} = 10 μm, and d) λ = 11.0 μm and D_{max} = 50 μm.

Fig. 5 shows plots of the scattering phase function for each of the 6 ice crystal habits in the single-scattering database. The phase functions are shown for ice crystal maximum dimensions of 10 and 50 μm at wavelengths of 8.55 and 11.0 μm. The strong forward peak of the phase function is evident for all habits, and is due to diffraction of light around the ice crystal. For larger particles, the magnitude of the forward peak is greater compared to that of small particles since higher amounts of energy are incident

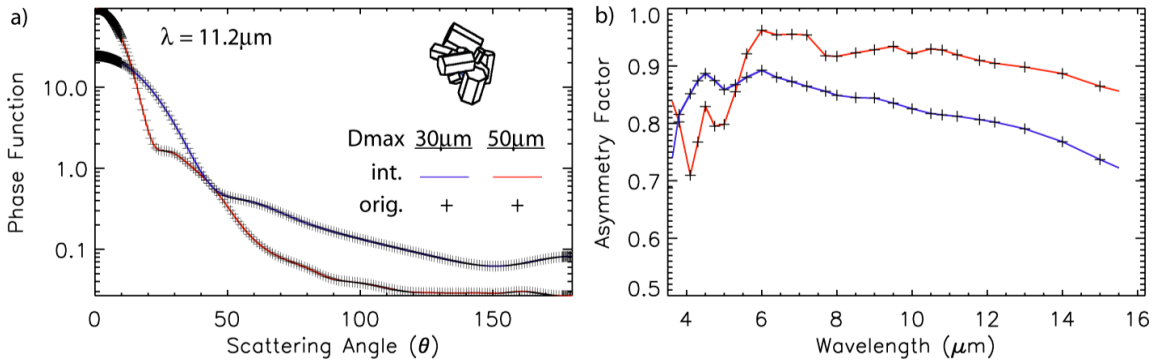

Fig. 6. Comparison of interpolated (line) and original (+) single-scattering databases for aggregates with D_{max} of 30 and 50 μm at a wavelength of 11.2 μm. Plots show comparisons of a) scattering phase function and b) asymmetry factor.

onto the broader surface area of the larger scattering particle, resulting in higher amounts of diffracted energy. For radiative transfer calculations, the forward peak must be truncated. Details of various truncation methods are given in section 2.5.

Comparisons of the interpolated and original single-scattering databases are made for quality assessment. Fig. 6a shows the interpolated phase functions at 11.2 μm for aggregate ice crystals at two sizes; 30 μm in blue, and 50 μm in red. The original phase functions at these wavelengths are over-plotted at each of the 498 originally computed scattering angles. Fig. 6b compares the interpolated and original asymmetry factor for the same sized aggregate ice crystals at 11.2 μm. The figures show that the single-scattering properties from the interpolated and original databases are in full agreement. Calculations were also performed using the IGOM for large size parameters, and these results compared well with the interpolated database. The solutions were not exact however, as the interpolated database originates from the composite method.

2.4 Bulk-Scattering Properties Computation

In nature, cirrus clouds cover a range of more complex ice crystal habits than the simplified morphologies used in computation of the single-scattering properties. For application to global remote sensing, a more realistic characterization of cirrus clouds, other than assuming a single habit at a single size, is required to perform retrievals of microphysical and optical properties. A representation of cirrus clouds in a RTM is defined by bulk-scattering properties, which relate the effective size of ice crystals within a modeled cirrus cloud, to their scattering and absorption properties. The effective size depends solely on the particle size distributions (PSDs) and habit distributions used, inferred from in-situ data, while the bulk-scattering properties computed for each effective size depend on these distributions, as wells as the incident wavelength and satellite instrument they are computed for. This section first outlines the in-situ data that defines the PSDs and habit distributions used, as a summary of Baum *et al.* [4], [6], [7]. We then detail the methods used to calculate effective size and the bulk-scattering properties for the IASI instrument, followed by an analysis of the results.

2.4.1 Inference of Particle Size and Habit Distributions

The application of a single cirrus cloud model to represent globally observed cirrus clouds is an extremely large simplification. Field campaigns have collected in-situ data covering many cirrus cloud regimes, including tropical and mid-latitude cirrus from deep convention and frontal boundaries, as well as artic cirrus. Observations from these field campaigns have revealed the vertical and horizontal inhomogeniety of cirrus clouds;

specifically, the distribution of particle size and habits. Five field campaigns used to infer PSDs and habit distributions come from Baum *et al.* [4]. These campaigns study both tropical and mid-latitude cirrus. To include observations from artic cirrus, we also use data collected during Surface Heat Budget of the Arctic Ocean (SHEBA) experiment [45].

From Baum *et al.* [4], two field campaigns which study tropical cirrus clouds are used: the Kwajalein Experiment (KWAJEX) in the Marshall Islands, and the Cirrus Regional Study of Tropical Anvils and Cirrus Layers (CRYSTAL) Florida Area Cirrus Experiment (FACE) off the coast of Nicaragua. The primary objective of KWAJEX was for validation of the Tropical Rainfall Measuring Mission (TRMM). Flights through deep convection initiated cirrus were conducted on a University of North Dakota Cessna Citation carrying a high-volume precipitation spectrometer (HVPS) probe and a cloud particle imager (CPI). The HVPS has a resolution of 0.2 mm and works well for measuring large particles, however measurements of PSDs with the CPI are unreliable and the instrument data is only used to analyze ice crystal morphology [42]. In CRYSTAL-FACE, the same Citation along with a NASA WB57 collected data from cirrus with a video ice particle sampler (VIPS) to measure PSDs from 20-200 μm.

Data for mid-latitude cirrus was collected during three field campaigns: the First International Satellite Cirrus Climatology Project Regional Experiment (FIRE-I) over Madison, WI in 1986, FIRE-II over Coffeyville, KS in 1991, and the Atmospheric Radiation Measurement Program (ARM) over Lamont, OK in 2000 [20]. National Center For Environmental Research (NCAR) aircraft were used in FIRE-I, while

balloon-borne replicators were used to collect data in FIRE-II, and the University of North Dakota Citation was used for observations at the ARM site. The balloon-borne replicator used in FIRE-II measured PSDs and imaged habits from 10 to 1000 μm at 2 μm resolution [21]. The habit imagery showed dependency of ice crystal habit on cloud temperature. Ice crystals at temperatures colder than -55° C were generally spherical with facets (droxtals), while ice crystals at temperatures around -50° C were pristine columns and plates. Polycrystals such as bullet rosettes existed in cloud layers between -40° and -45° C, while aggregates were predominate in the growth layers warmer than -40° C.

The particle size distributions were measured continuously and averaged every 30m of the aircraft spiral descents through the cloud layer, and averaged every 300m of balloon ascent through the cloud layer. The PSDs were then fit to a gamma size distribution following [19] of the form

$$n(D) = N_0 D^{\mu} e^{-\lambda D}, \tag{7}$$

where D is the maximum dimension, $n(D)$ is the particle number concentration per unit volume, N_0 is the intercept, λ is the slope, and μ is the dispersion. To ensure that only PSDs containing particles in the ice phase are used, the data was filtered for PSDs where the cloud temperature was colder than -25° C. After filtering, 1117 PSDs of the original 4000 remain.

Along with the particle size distributions, a habit distribution is also required to compute the bulk-scattering properties. This habit distribution may be limited to one single habit, or a mix of habits whose percentage is a function of maximum dimension.

To derive a habit distribution for the cirrus model, Baum *et al.* [4] configured a mix of habits to calculate Ice Water Content (IWC) and Median Mass Diameter (D_m). D_m is defined as the diameter where half of the total mass within a PSD resides in particles smaller than the diameter, and the other half resides in particles with larger diameters. The calculated IWC and D_m were then compared to the values derived from the in-situ data. Assuming a habit distribution composed of 100% droxtals for $D_{max} < 60$ μm, and 100% aggregates for $D_{max} > 60$ μm, IWC and D_m both over-estimated derived values from in-situ data. The habit distribution was then adjusted, keeping 100% droxtals for $D_{max} < 60$ μm, but changing $D_{max} > 60$ μm to 100% bullet rosettes. The results showed that calculated IWC under-estimated derived values from in-situ data, and over-estimated D_m. The best fit to the derived IWC and D_m from in-situ data is the habit distribution in Table 1. Along with computing the bulk-scattering properties for each individual habit, these properties will also be computed assuming the habit distribution from Baum *et al.* [4], from here to be referred as Baum v2.

2.4.2 Computation of Bulk-Scattering Properties

The process for computing the bulk-scattering properties for the ice cloud models is presented here. Seven ice cloud models are constructed for the IASI instrument. Six of these models are created with the assumption that the ice cloud contains only a single ice crystal habit, one for each ice crystal habit in the single-scattering properties database. The seventh ice cloud model is built assuming the Baum v2 habit distribution.

Table 1. Habit distribution from Baum *et al.* [4] listing the percentage of each habit with given maximum dimension.

Max. Dimension	Habit 1	Habit 2	Habit 3
$D_{max} < 60$	100% Droxtals		
$60 < D_{max} < 1000$	15% Bullet Ros.	50% Solid Col.	35% Plates
$1000 < D_{max} < 2000$	45% Hollow Col	45% Solid Col.	10% Aggregates
$2000 < D_{max}$	97% Bullet Ros.	3% Aggreates	

The 1902 PSDs from the previously mentioned in-situ data are used for each cirrus model.

The first step in calculating the bulk-scattering properties is computing an effective size of the ice crystals in the model cirrus cloud. Following Foot [13] and Francis *et al.* [14], the effective diameter is given by

$$D_e = \frac{3}{2}\frac{\int_{D_{\min}}^{D_{\max}}\left[\sum_{h=1}^{M} f_h(D)V_h(D)\right]n(D)dD}{\int_{D_{\min}}^{D_{\max}}\left[\sum_{h=1}^{M} f_h(D)A_h(D)\right]n(D)dD}, \tag{8}$$

where D is the maximum dimension, V is the particle volume, A is the particle area, $n(D)$ is the number concentration, and f_h is the habit fraction

$$\sum_{h=1}^{M} f_h(D) = 1, \tag{9}$$

where h is the habit type, M is the total number of habits in the distribution, and the summation over all habit percentages equals to one. The effective size is therefore

dependent on the habit fraction and also on the PSD. Given an assumed habit distribution, the use of each PSD in functional form will result in a computed value for D_e. To create the cirrus models, the computed D_e values are discretized into sizes between 10 and 180 μm at 10 μm increments. To calculate the bulk-scattering properties for each discrete D_e value, 10-20 PSDs which computed D_e to within about ± 2 μm of the discrete value, are used. For example from Baum *et al.* [7], to compute the bulk-scattering phase function,

$$\overline{P}(\theta,\upsilon) = \frac{\int_{D_{\min}}^{D_{\max}} \left[\sum_{h=1}^{M} P_h(\theta,D,\upsilon)\sigma_{sca,h}(D,\upsilon)f_h(D)\right] n(D)dD}{\int_{D_{\min}}^{D_{\max}} \left[\sum_{h=1}^{M} \sigma_{sca,h}(D,\upsilon)f_h(D)\right] n(D)dD}, \tag{10}$$

the integration is performed only for *n(D)*of select PSDs. The solutions using each PSD are then averaged together to give the scattering phase function. Other bulk-scattering properties are computed by the same manner, including the asymmetry factor

$$\overline{g}(\upsilon) = \frac{\int_{D_{\min}}^{D_{\max}} \left[\sum_{h=1}^{M} g_h(D,\upsilon)\sigma_{sca,h}(D,\upsilon)f_h(D)\right] n(D)dD}{\int_{D_{\min}}^{D_{\max}} \left[\sum_{h=1}^{M} \sigma_{sca,h}(D,\upsilon)f_h(D)\right] n(D)dD}. \tag{11}$$

Fig. 7 shows the bulk single-scattering phase functions for cirrus models with individual ice crystal habits, compared to the phase functions for the Baum v2 habit distribution. The phase functions are shown for an effective size of 30 μm at wavelengths of 4.1, 8.5 and 11.2 μm. Compared to the single-scattering phase functions, the bulk single-scattering phase functions appear smoother across the scattering angles, especially for droxtals and plates. This is a result of integrating over a number of PSDs

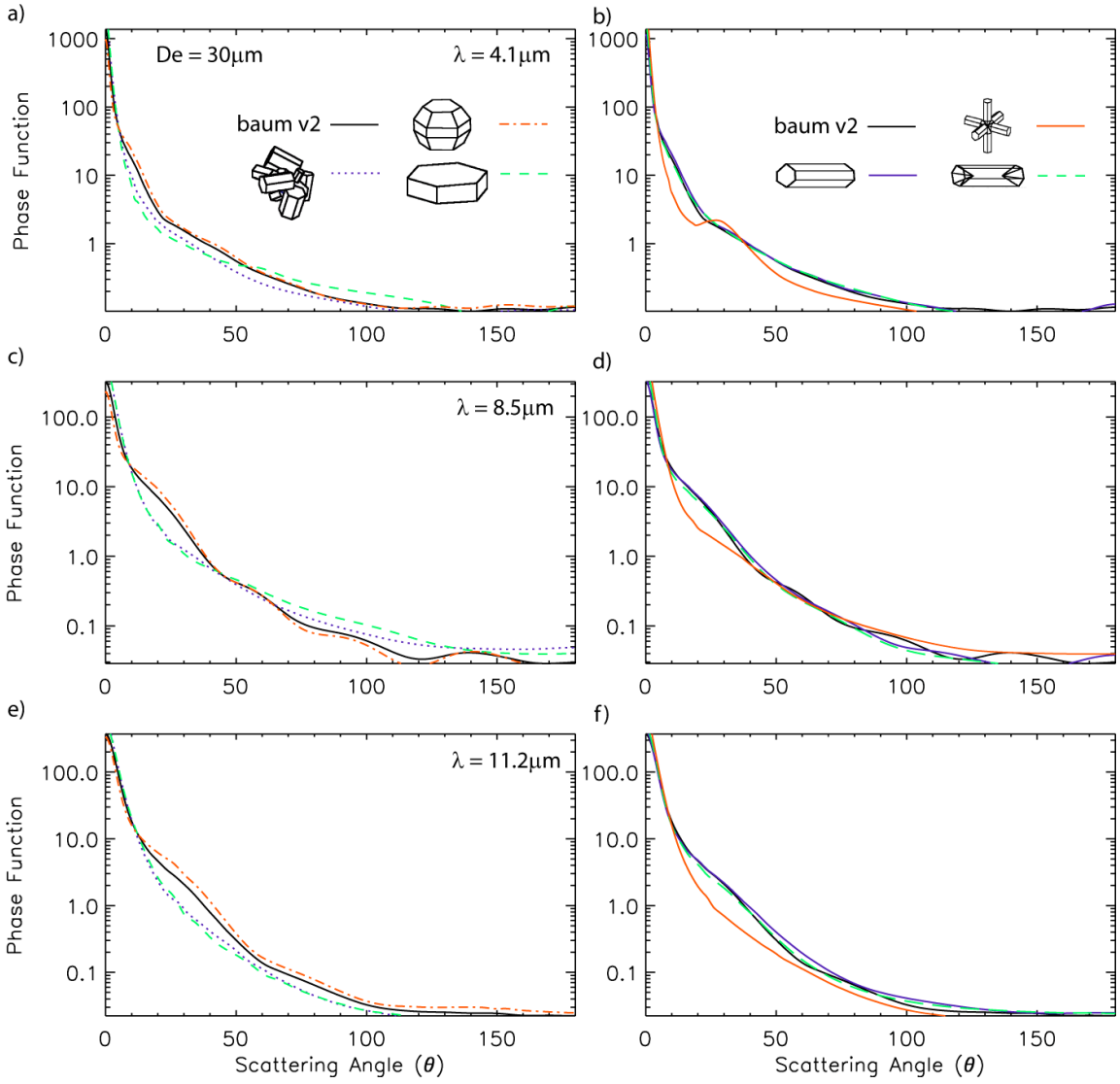

Fig. 7. Bulk single-scattering phase functions for 6 individual ice crystal habits compared with the Baum v2 for a D_e of 30 µm. Phase functions are plotted for wavelengths of a), b) 4.1 µm, c), d) 8.5µm and e), f) 11.2 µm.

which contain a quantity of large particles. Comparing the bulk-scattering phase functions among the habit distributions, the Baum v2 phase functions fall between the phase functions of the individual habits. This is to be expected as the Baum v2 bulk-scattering properties are weighted by individual ice crystals given in the habit fraction.

Bulk-extinction efficiency, single-scattering albedo, and asymmetry factor are shown for the six individual ice crystal habits and the habit distribution of Baum v2 in Fig. 8 for an effective size of 30 μm, as a function of wavelength. As with the single-scattering properties for smaller sized particles, there is still variability in the bulk-scattering properties across the IASI spectrum, demonstrating that sensitivity to wavelength still exists after averaging. It is these differences that remote sensing techniques rely upon to perform retrievals of cirrus cloud microphysical and optical properties. However, the variability between the ice crystal habits has decreased substantially compared with the single-scattering property database. As with the scattering phase functions, the Baum v2 bulk-scattering properties fall between the values of bulk-scattering properties for the individual ice crystal habits.

For increased effective sizes (Figs. 9, 10), both the variation across the IASI spectrum, and among the ice crystal habits is decreased substantially. In fact, for an effective size of 100 μm, the bulk-scattering properties are nearly constant for all wavelengths and ice crystal habits. Thus, as effective size increases, the habit or habit distribution assumed in the ice cloud model becomes less important. However, the ability to infer cirrus cloud properties from clouds with effective diameters larger than

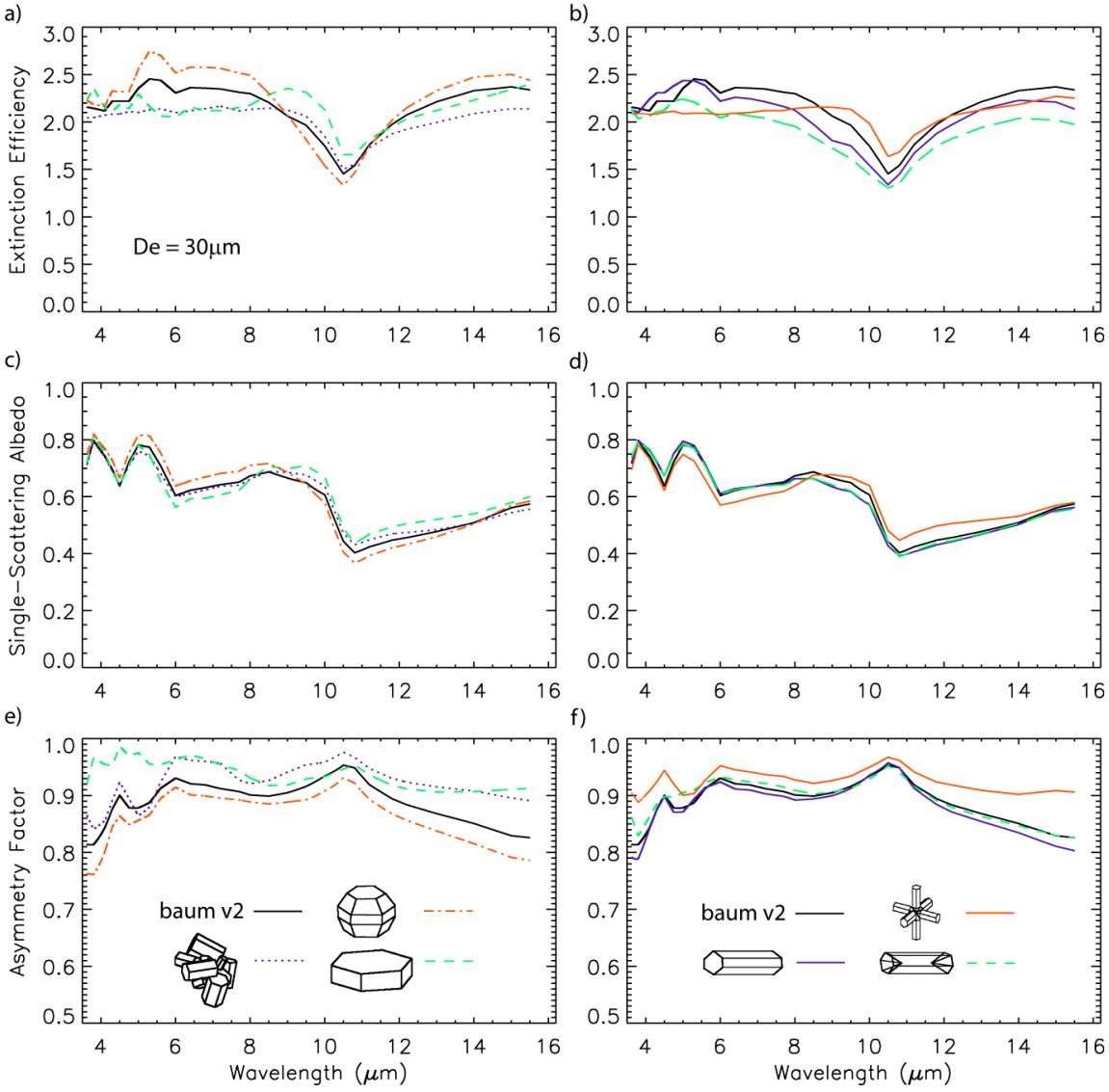

Fig. 8. Bulk-scattering properties for 6 individual ice crystal habits compared with properties from Baum v2 habit distribution with an effective size of 30 μm as a function of wavelength. Plots shown for a), b) extinction efficiency, c), d) single-scattering albedo, and e), f) asymmetry factor.

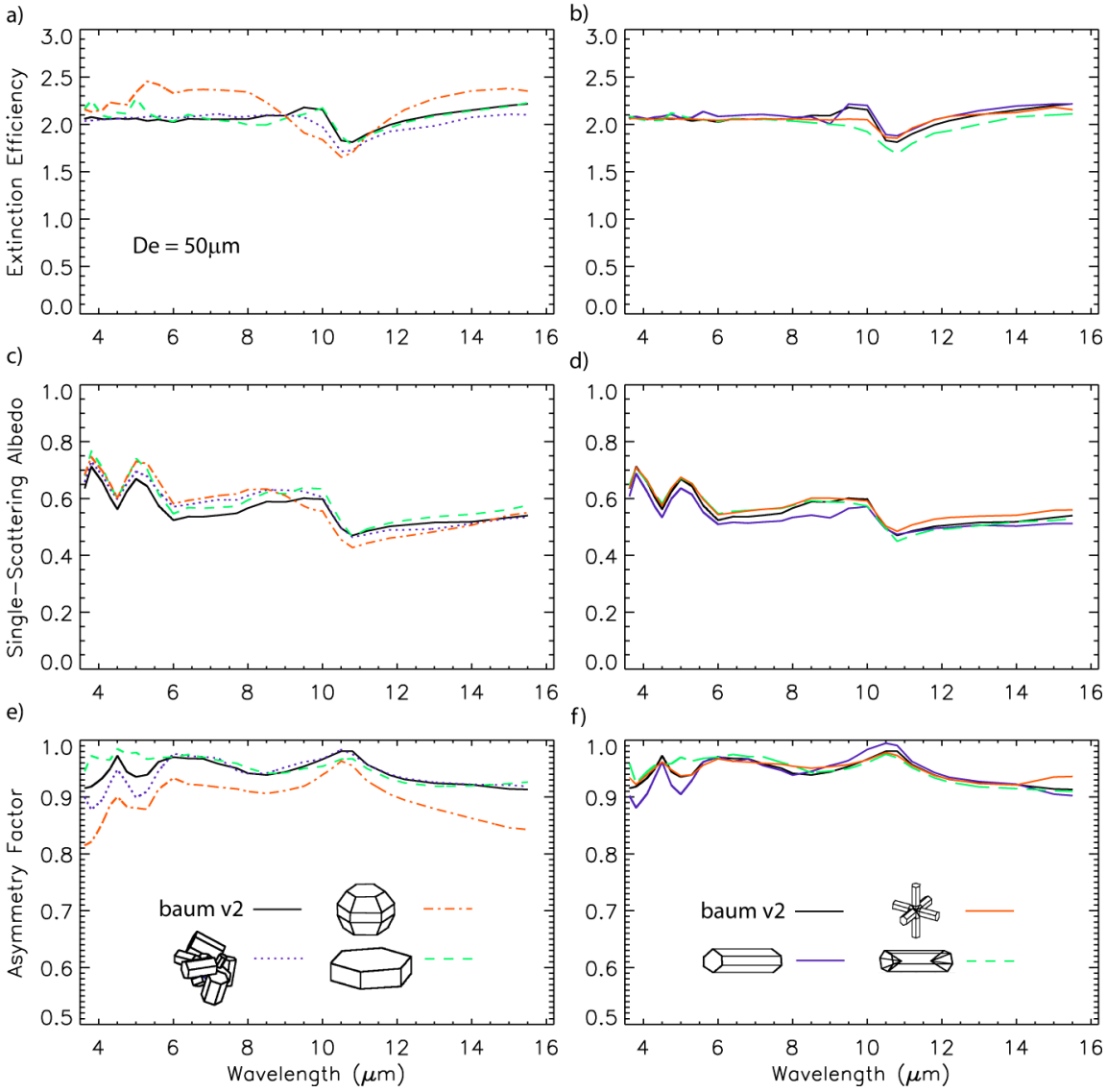

Fig. 9. Bulk-scattering properties for 6 individual ice crystal habits compared with properties from Baum v2 habit distribution with an effective size of 50 μm as a function of wavelength. Plots shown for a), b) extinction efficiency, c), d) single-scattering albedo, and e), f) asymmetry factor.

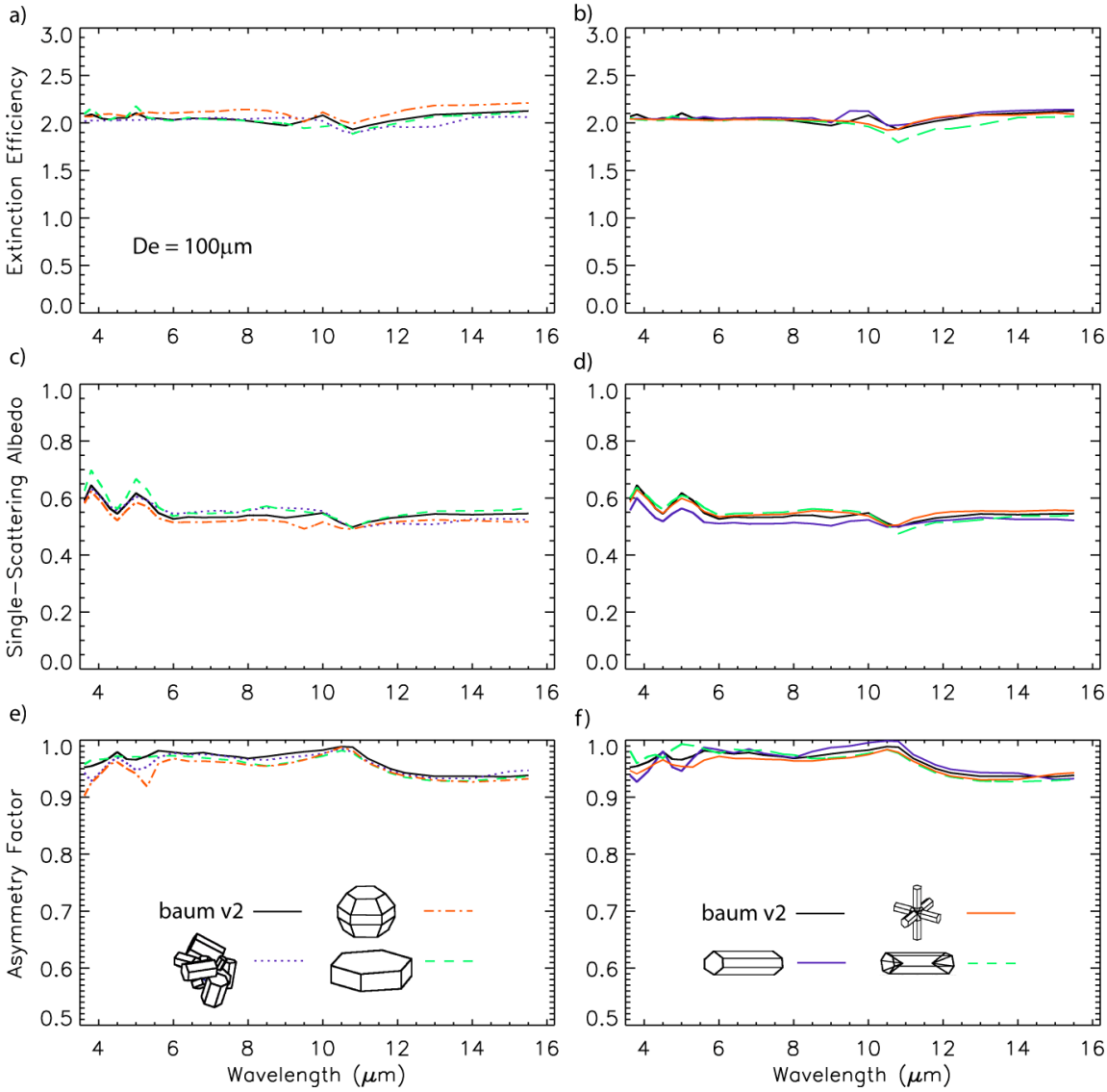

Fig. 10. Bulk-scattering properties for 6 individual ice crystal habits compared with properties from Baum v2 habit distribution with an effective size of 100 μm as a function of wavelength. Plots shown for a), b) extinction efficiency, c), d) single-scattering albedo, and e), f) asymmetry factor.

50 μm may be difficult because of decreased sensitivity to particle size as IR absorption by the larger ice crystals dominates.

2.5 IASI Spectral Simulations

To evaluate the sensitivity that the assumed ice cloud model may have on simulated cloudy radiances at wavelengths throughout the IASI spectrum, simulations are performed for a variety of cirrus clouds using each of the ice cloud models.

To simulate the infrared radiances at TOA we implement the discrete ordinates radiative transfer (DISORT) model [41]. DISORT computes the monochromatic radiance for plane-parallel, adjacent atmospheric layers by solving the radiative transfer equation

$$\mu \frac{dI_\nu(\tau_\nu,\mu,\phi)}{d\tau} = I_\nu(\tau_\nu,\mu,\phi) - S_\nu(\tau_\nu,\mu,\phi), \tag{12}$$

where $I_\nu(\tau_\nu,\mu,\phi)$ is the monochromatic intensity in direction μ, ϕ at optical thickness τ, μ is the cosine of the solar zenith angle (cosθ) and $S_\nu(\tau_\nu,\mu,\phi)$ is the source function

$$S_\nu(\tau_\nu,\mu,\phi) = \frac{\omega_\nu(\tau_\nu)}{4\pi}\int_0^{2\pi}\int_{-1}^{1} P_\nu(\tau_\nu,\mu,\phi;\mu',\phi')d\mu' d\phi' \tag{13}$$

$$\times \quad I_\nu(\tau_\nu,\mu,\phi) + Q_\nu(\tau_\nu,\mu,\phi),$$

where $\omega_\nu(\tau_\nu)$ is the single-scattering albedo, $P_\nu(\tau_\nu,\mu,\phi;\mu',\phi')$ is the scattering phase function and $Q_\nu(\tau_\nu,\mu,\phi)$ is the source term. It is the nature of ice crystals to have a very strong forward peak of the phase function, thus requiring hundreds of terms in the Legendre polynomial expansion to accurately capture the distribution of scattered

intensity at large scattering angles in the forward calculations. At solar and NIR wavelengths, the forward peak is due to large amounts of diffracted (delta-diffraction) and transmitted (delta-transmission) energy around and through the particle. However, at highly absorbing IR wavelengths, the delta-transmission contribution is small and can be neglected. For use in radiative transfer calculations, the Legendre polynomial expansion coefficients are calculated using the δ-fit truncation method [23] which removes the forward peak and smooths out the phase function. Thus, only a limited number of expansion coefficients are required to express the phase function, allowing for more computational efficiency. The Legendre polynomial expansion series is given by

$$P(\theta) = \sum_{\ell=0}^{N} x_\ell p_\ell(\cos\theta), \tag{14}$$

where x_ℓ is the ℓ^{th} expansion coefficient,

$$x_\ell = \frac{2}{2L+1} \int p_\ell(\cos\theta) P_{ac}(\theta) d(\cos\theta), \tag{15}$$

p_ℓ is the ℓ^{th}-order Legendre polynomial and $P_{ac}(\theta)$ is the actual phase function. The δ-fit method employs a least-squares fitting procedure to generate the coefficients c_ℓ by minimizing the relative difference ε between the actual and approximated phase function $P'(\theta_i)$

$$\varepsilon = \sum_i w_i \left(\frac{P'(\theta_i)}{P_{ac}(\theta_i)} - 1 \right)^2 \tag{16}$$

$$P'(\theta_i) = \sum_{\ell=0}^{N_{str}} c_\ell p_\ell(\cos\theta_l), \tag{17}$$

where θ_i is the scattering angle, w_i is the weight for each scattering angle, and $p_\ell(\cos\theta_l)$ is the Legendre polynomial for N streams of radiation. In our model, 32 streams are used for the expansion. The coefficients are computed by solving the least-squares fitting problem $\partial\varepsilon/\partial c_k = 0 \ (k = 0,N)$

$$\sum_{i=0} \frac{p_k(\cos\theta_i)}{P_{ac}(\theta_i)} w_i \left(\sum_{\ell=0}^{N_{str}} \frac{c_\ell p_\ell(\cos\theta_i)}{P_{ac}(\theta_i)} - 1 \right) = 0, \tag{18}$$

and the normalized phase function is then

$$P_{\delta-fit}(\theta_i) = \frac{1}{1-f} P'(\theta_i). \tag{19}$$

Along with the phase function, the diffracted energy contributes to other single-scattering properties and must be removed. Through a mathematical process known as the Similarity Principle, the portion of energy in the forward peak of the phase function, *f*, is used for scaling the optical thickness,

$$\tau' = (1 - f\omega)\tau, \tag{20}$$

single-scattering albedo,

$$\omega' = \frac{(1-f)\omega}{1-\omega f}, \tag{21}$$

and the asymmetry factor,

$$g' = \frac{g-f}{1-f}, \tag{22}$$

where τ is the original optical thickness, ω the original single-scattering albedo, and g the original asymmetry factor.

Observed IR radiances at TOA are also sensitive to absorbing gases in the atmosphere, and the model must account for any attenuation due to the concentration of these gases for each simulated wavelength. Our model uses pressure, temperature, water vapor and ozone profiles from a standard tropical atmosphere [26]. To compute the clear-sky IR transmission the rigorous line-by-line method is used. Line-by-line calculates the absorption coefficient, k

$$k_{\upsilon}(p,T) = \sum_{i} S_i(T) f_{i,\upsilon}(p,T), \tag{23}$$

where p is the pressure, T is the temperature, S is the line intensity, and f is the line shape factor for the i^{th} absorption line at a specified wavenumber, υ. The transmittance can then be solved for by integrating over a wavenumber interval,

$$T_{\Delta\upsilon}(u,p,T) = \int_{\Delta\upsilon} e^{-k_{\upsilon}(p,T)u} \frac{d\upsilon}{\Delta\upsilon}, \tag{24}$$

where u is the pathlength through the atmospheric layer.

The above model is used to simulate IR radiances for all 8461 wavelengths in the IASI spectral domain. Bulk-scattering properties each of the 7 ice cloud models are inserted into the atmosphere at a fixed height and geometric thickness, and simulated radiances are performed for clouds with visible optical thicknesses of 0.1, 1.0, 2.0, and 5.0, and effective diameters of 30, 50, and 100 μm. Fig. 11 shows the simulated IASI spectrum for a cloud with D_e equal to 30 μm and optical thicknesses of 0.1, 1.0, 2.0, and 5.0 for each of the cirrus models composed with individual ice crystal habits. It is clear from Fig. 11 that for small to moderately optically thick clouds, there is good sensitivity of the simulated spectra to the cirrus cloud properties as well as background atmosphere,

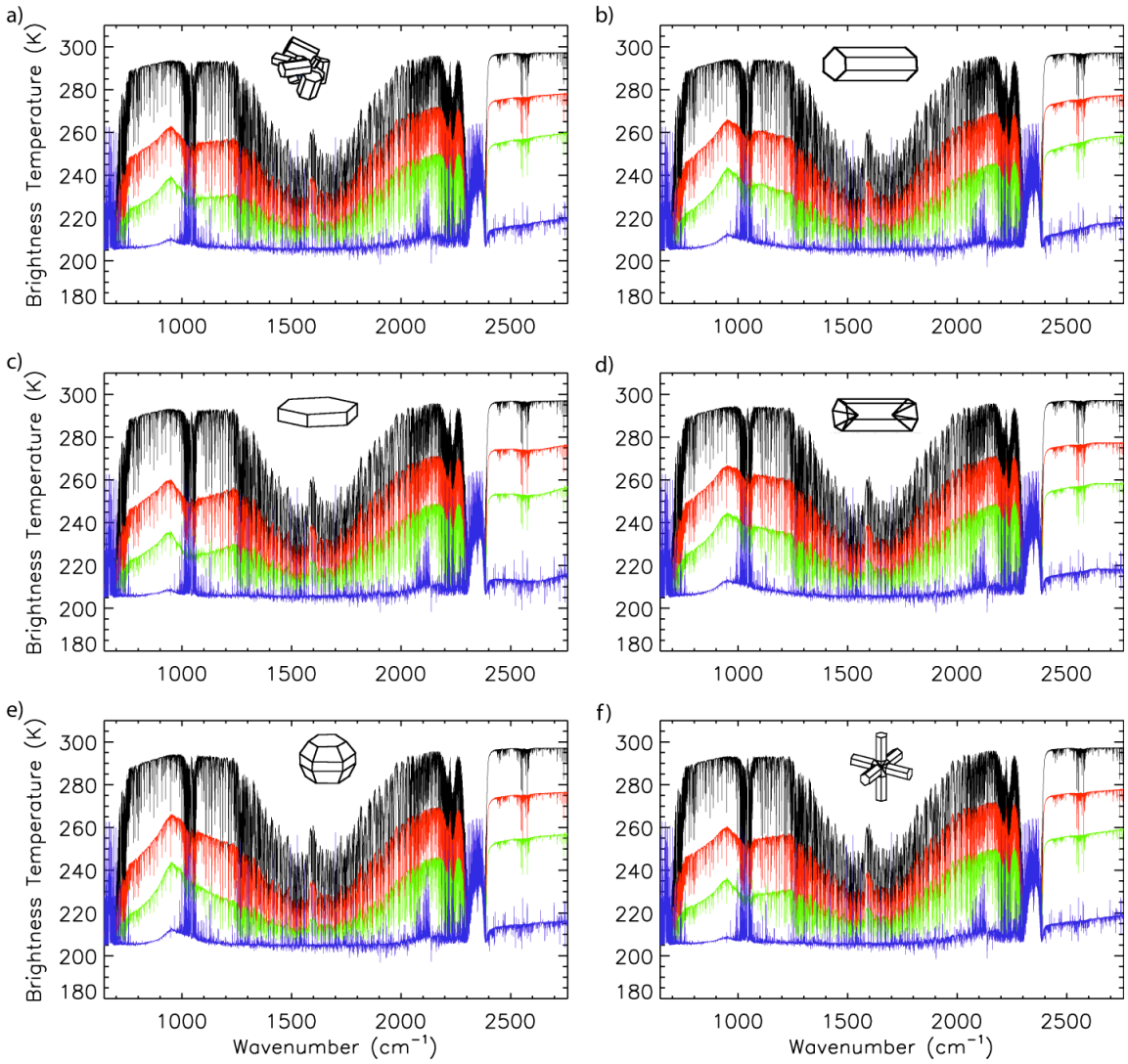

Fig. 11. Simulated brightness temperatures of clouds with an effective diameter of 30 µm for optical thickness of 0.1 (black), 1.0 (red), 2.0 (green), and 5.0 (blue). Simulations are shown for 6 ice cloud models of individual ice crystal habits, a) aggregates, b) solid columns, c) plates, d) hollow columns, e) droxtals, and f) bullet rosettes.

noting the O_3 and CO_2 absorption bands around 9.6 and 13.2 μm, respectively, as well as the H_2O continuum from 1200 – 2100 cm^{-1}. The region between 790 and 960 cm^{-1} has been investigated for sensitivity to ice crystal effective size, while the spectral region between 1070 and 1135 cm^{-1} has been used to retrieve optical thickness [24], [48]. From Fig. 11, we see that these regions are also sensitive to ice crystal habit, as differences of brightness temperatures are apparent, especially for clouds with optical thicknesses around 1.0 and 2.0. For optically thicker clouds, the simulated brightness temperatures are nearly constant for all wavelengths, except in the strongest absorption bands, as the clouds radiate as a blackbody. Thus for optical thickness of 5 or greater, sensitivity to ice crystal effective size is lost, and the assumption of ice crystal habit becomes less important.

Fig. 12 shows a simulation of the IASI spectrum using the ice cloud model with the assumption of the habit distribution from Baum *et al.* [4]. The simulations are carried out for clouds with effective diameters of 30, 50, and 100 μm and for optical thicknesses of 0.1, 1.0, 2.0, and 5.0. Emphasis on the importance of the 790 – 960 cm^{-1} spectral region for inferring ice cloud effective size is shown in Figs. 12b, d, and f. For optical thicknesses of 1.0 and 2.0, the slope of the simulated brightness temperatures in this region decreases with increasing effective diameter. The slope is positive for each plot, as the simulated brightness temperature becomes colder as IR absorption increases with decreasing wavenumber. As particle size increases, absorption becomes even greater around 960 cm^{-1}, leading to the decrease of slope. Since this region falls within the

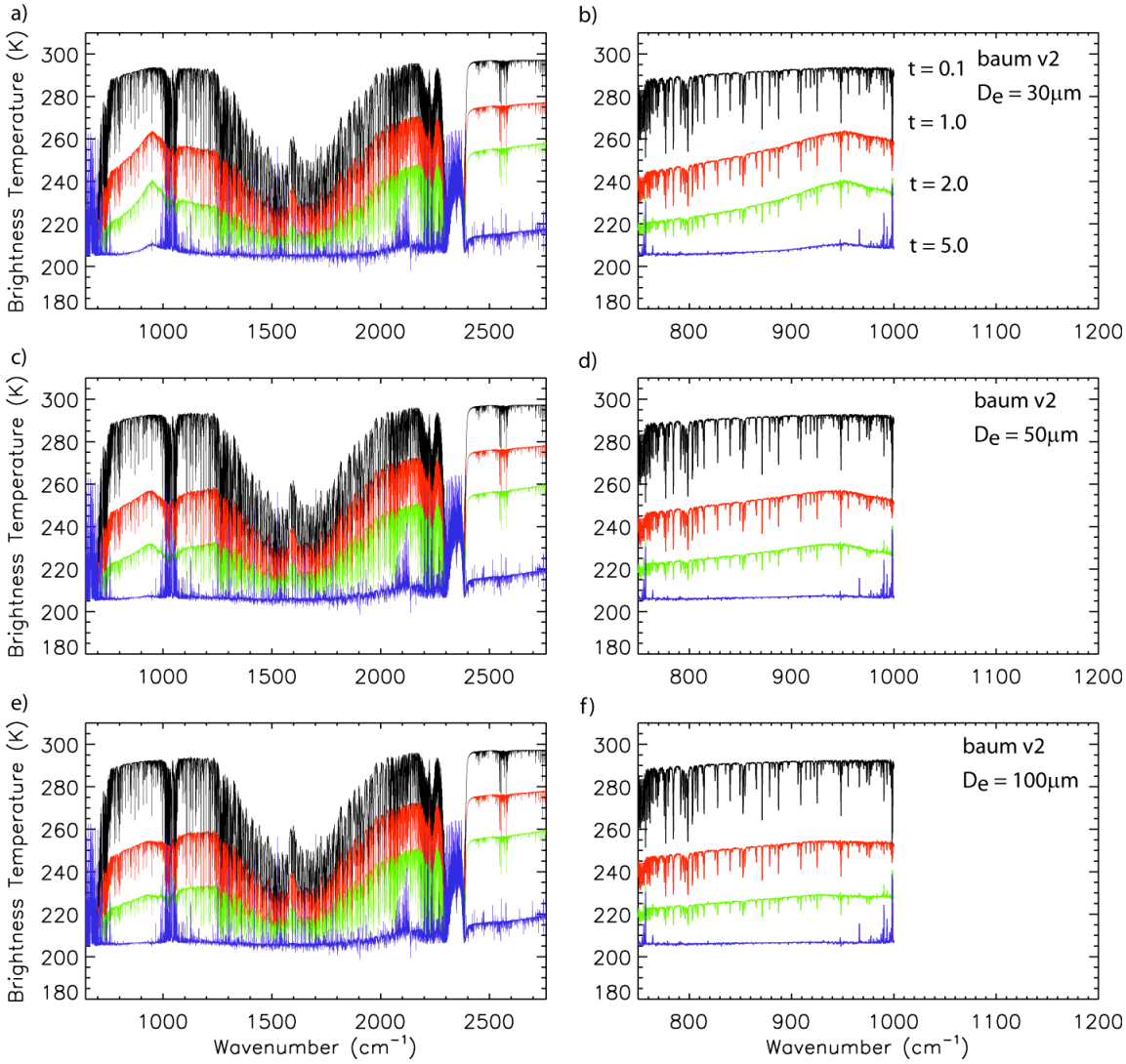

Fig. 12. Simulated brightness temperatures of clouds with the habit distribution of Baum *et al.* [4] for clouds with effective diameters of 30, 50 and 100 µm and optical thicknesses of 0.1, 1.0, 2.0, and 5.0. Simulations are shown for a), c), e) the IASI spectrum and b), d), f) the spectral region between 700 and 1000 cm^{-1}.

atmospheric window, it is preferable to use this information for inference of ice crystal effective size. However, for large optical thickness or effective size, absorption of the outgoing thermal emission causes saturation in the spectral region and sensitivity to cirrus cloud properties are lost.

In Fig. 13, the sensitivity of the simulated IASI spectrum to the ice cloud model used is shown. Brightness temperature differences between the cirrus model using the Baum v2 habit distribution, and the cirrus models for individual ice crystal habits, are plotted as a function of wavenumber. Each simulation is carried out for a cloud with an optical thickness of 2.0 and effective diameter of 30 μm. Brightness temperature differences between the Baum v2 model and each individual habit model range from 2 – 8 K across the spectrum. These differences also occur in the spectral regions which may be used to infer cirrus cloud properties. Again, as optical thickness and effective size increase, the brightness temperature differences decrease as the assumed habit distribution becomes less important.

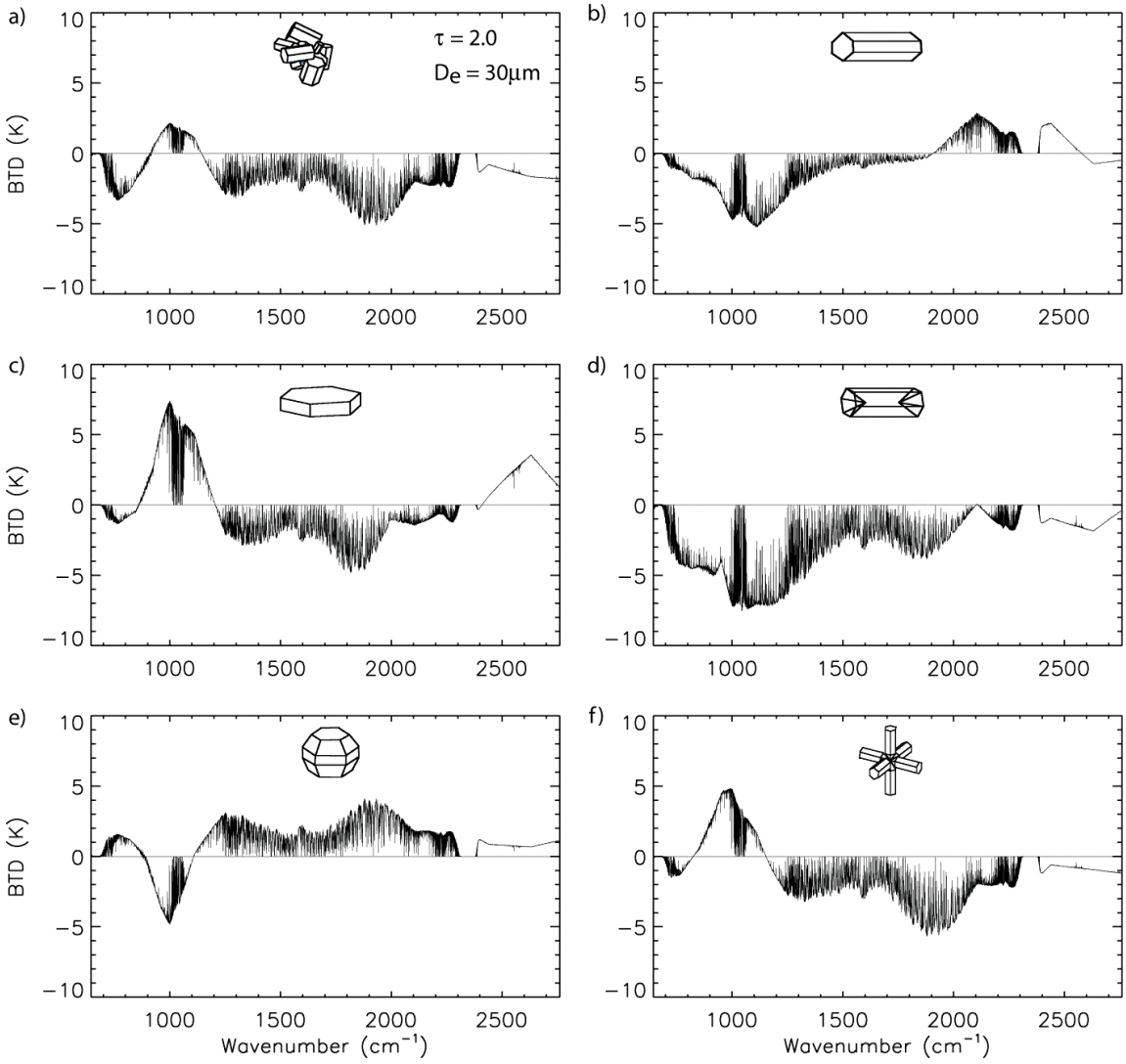

Fig. 13. Difference of the simulated brightness temperatures of clouds using the Baum *et al.* [4] habit distribution and individual ice crystals. Differences are shown for a) aggregates, b) solid columns, c) plates, d) hollow columns, e) droxtals, and f) bullet rosettes. All clouds have an optical thickness of 2.0 and an effective diameter of 30 µm.

3. SENSITIVITY OF INFRARED BRIGHTNESS TEMPERATURES TO CLOUD TEMPERATURE

In this section we investigate the sensitivity of a model to retrieve cirrus cloud effective size and optical thickness, which utilizes infrared brightness temperatures at 8.5 and 11.0 μm, to cloud temperature. The basis for choosing these wavelengths for the retrieval model is found by examining the differences in ice scattering and absorption at these channels, as shown previously in Fig. 2b, the refractive index of ice (imaginary part). For a cirrus cloud at a given height and geometric thickness, the effective emitting temperature at both wavelengths is a function mainly of the ice cloud effective particle size, optical thickness at each wavelength, and the temperature profile through out the cloud layer. For cirrus clouds composed of small ice crystals and small to moderate optical thickness, energy at 8.5 and 11.0 μm is transmitted through the cloud to top-of-atmosphere. However, energy at 11.0 μm is more strongly absorbed by ice crystals than at 8.5 μm, and it can be expected that brightness temperatures are therefore colder at 11.0 μm above a cirrus cloud. This brightness temperature difference ($BTD_{8.5\text{-}11.0}$) may then be used to infer cirrus cloud properties, where 8.5 μm is sensitive to the effective size of ice crystals, and 11.0 μm is mainly a function of optical thickness.

As the ice crystals increase in size, or the cloud becomes more optically thick, energy at 8.5 μm is increasingly absorbed, and $BTD_{8.5\text{-}11.0}$ approaches zero as the cloud emits at an effective temperature close to the cloud temperature. However, not only do the cirrus cloud microphysical and optical properties have an effect on the brightness

temperatures at these IR wavelengths, but the brightness temperatures are also sensitive to the cloud top temperature and cloud base temperature as determined by the height and geometric thickness of the cirrus cloud. It is the purpose of this theoretical study to investigate this sensitivity on cloud temperature to the bi-spectral $BTD_{8.5\text{-}11.0}$ retrieval method.

3.1 Methodology

To investigate the sensitivity of the bi-spectral $BTD_{8.5\text{-}11.0}$ retrieval approach to cloud temperature, we have developed a model to simulate brightness temperatures over cirrus clouds composed of different properties for a variety of cloud top temperatures and cloud layer temperatures. Brightness temperatures for each case are computed using the DISORT model.

3.1.1 Gaseous Absorption

Similar to our IASI spectral simulations in Section 2.5, we begin with the standard tropical atmosphere [26] over a Lambertian, ocean surface. The atmosphere is divided into 35 levels and 34 layers, and contains information about pressure, temperature, water vapor, and ozone profiles. Again, absorbing molecules such as CO_2, H_2O vapor, O_3, CH_4, and N_2O may attenuate any upwelling radiance from the surface. Not compensating for gaseous absorption in the atmosphere could affect brightness temperature simulations by as much as a few Kelvin or more depending on the wavelength. However, instead of employing the line-by-line method, atmospheric

transmittance for each layer is estimated by using the correlated *k*-distribution method [15]. Unlike the line-by-line method, the *k*-distribution expresses the absorption coefficient, *k*, in terms of a probability distribution function, *h(k),* the likelihood a *k* value will be found within a given spectral interval, $\Delta\upsilon$. Integrating over all possible values of *k* in a homogeneous pathlength, *u*, the transmittance can be calculated by

$$T_\upsilon(u) = \int_0^\infty e^{-ku} h(k)dk. \tag{25}$$

It is more practical to express *h(k)* as a cumulative probability distribution function,

$$g(k) = \int_0^k h(k)dk, \tag{26}$$

where *g(k)* and its inverse

$$k(g) = g'(k), \tag{27}$$

are monotonically increasing and smooth functions. Applied to an inhomogeneous pathlength between z_1 and z_2, the transmittance is found by

$$T_\upsilon = \int_0^\infty \exp\left[-\int_{z_1}^{z_2} k(\upsilon, P, T)_g \rho dz\right] dg, \tag{28}$$

where the *k* value at any given pressure, *P*, or temperature, *T*, will be correlated with that of a *k* value at a specified reference pressure or temperature.

Our model uses the correlated *k*-distribution routines described by Kratz [25]. These routines were constructed for MODIS channels 29 and 31, which correspond to 8.5 and 11.0 μm. Theoretical computations for clear-sky transmittances have been performed within our standard tropical atmosphere and compared with line-by-line results to within 1% (Bryan Baum, personal communication).

3.1.2 Cirrus Models

For simulated brightness temperatures over a cloud layer, MODIS specific single-scattering property ice cloud models have been developed by Baum *et al.* [6], the basis of which is discussed in Section 2.5. The calculation of the effective diameter, D_e, follows Eq. 8. However, the bulk-scattering properties such as the phase function, $\overline{P}(\theta)$, are weighted by the spectral response function and follow the form from Baum *et al.* [6]

$$\overline{P}(\theta) = \frac{\int_{\lambda_1}^{\lambda_2} \int_{D_{\min}}^{D_{\max}} \left[\sum_{h=1}^{M} P_h(\theta, D, \lambda) \sigma_{sca,h}(D, \lambda) f_h(D) \right] \times n(D) F_s(\lambda) B(\lambda) dD d\lambda}{\int_{D_{\min}}^{D_{\max}} \left[\sum_{h=1}^{M} \sigma_{sca,h}(D, \lambda) f_h(D) \right] \times n(D) F_s(\lambda) B(\lambda) dD d\lambda}, \tag{29}$$

where λ is the wavelength, $P_h(\theta, D, \lambda)$ is the phase function of a single habit, $\sigma_{sca,h}(D, \lambda)$ is the scattering cross section, $F_s(\lambda)$ is the spectral response function, and $B(\lambda)$ is the Planck function. Again, for the development of the cirrus models, the habit distribution in Table 1 is assumed. As described previously, the truncated phase function is then approximated by Legendre polynomial expansion for input into DISORT.

3.2 Sensitivity to Cloud Top Temperature

We first investigate the sensitivity of simulated infrared brightness temperatures (BTs) at TOA to cloud top temperature in the standard tropical atmosphere over an ocean surface. The standard tropical atmosphere contains 34 atmospheric computational

layers. A single-layer cloud is inserted into 5 cloud top heights ranging from 8-16 km with a cloud geometric thickness fixed at 1 km. Brightness temperatures are simulated with DISORT for clouds with an effective diameter of 30, 50 and 100 μm for optical thicknesses between 0.1 and 10.

Figs. 14a, c, and e show simulated BTs at 8.5 and 11.0 μm for clouds with an effective diameter of 30, 50 and 100 μm, respectively, as a function of optical thickness. The cloud top temperature ranges from 197 K at 16 km to 250 K at 8 km, while the surface temperature is 300 K. Figs. 14b, d, and e are plots of the 8.5 – 11.0 μm brightness temperature difference ($BTD_{8.5\text{-}11.0}$) for each cloud type as a function of optical thickness. Comparing the simulations, there are greater BTDs for clouds with smaller effective diameters, however, as cloud top temperature increases, the BTDs decrease. If we depend on the $BTD_{8.5\text{-}11}$ as our retrieval method, it may become increasingly difficult to infer effective size for diameters larger than 50 μm because the $BTD_{8.5\text{-}11.0}$ approaches zero, even for the highest (coldest) cloud tops.

It is also evident from Fig. 14 that for optically thin clouds ($\tau_{0.55} < 1$), there is not much sensitivity to cloud top temperature; $BTD_{8.5\text{-}11}$ is on the order of 3 K and may be too small to infer cloud properties with any confidence. In these regions of small optical thickness, transmission from upwelling radiance below the cloud is dominant at each wavelength. For clouds of moderate optical thickness, our peak $BTD_{8.5\text{-}11}$ is around $\tau_{0.55} = 3$. In this region, absorption of the 11.0 μm radiance is greater than at 8.5 μm. As the

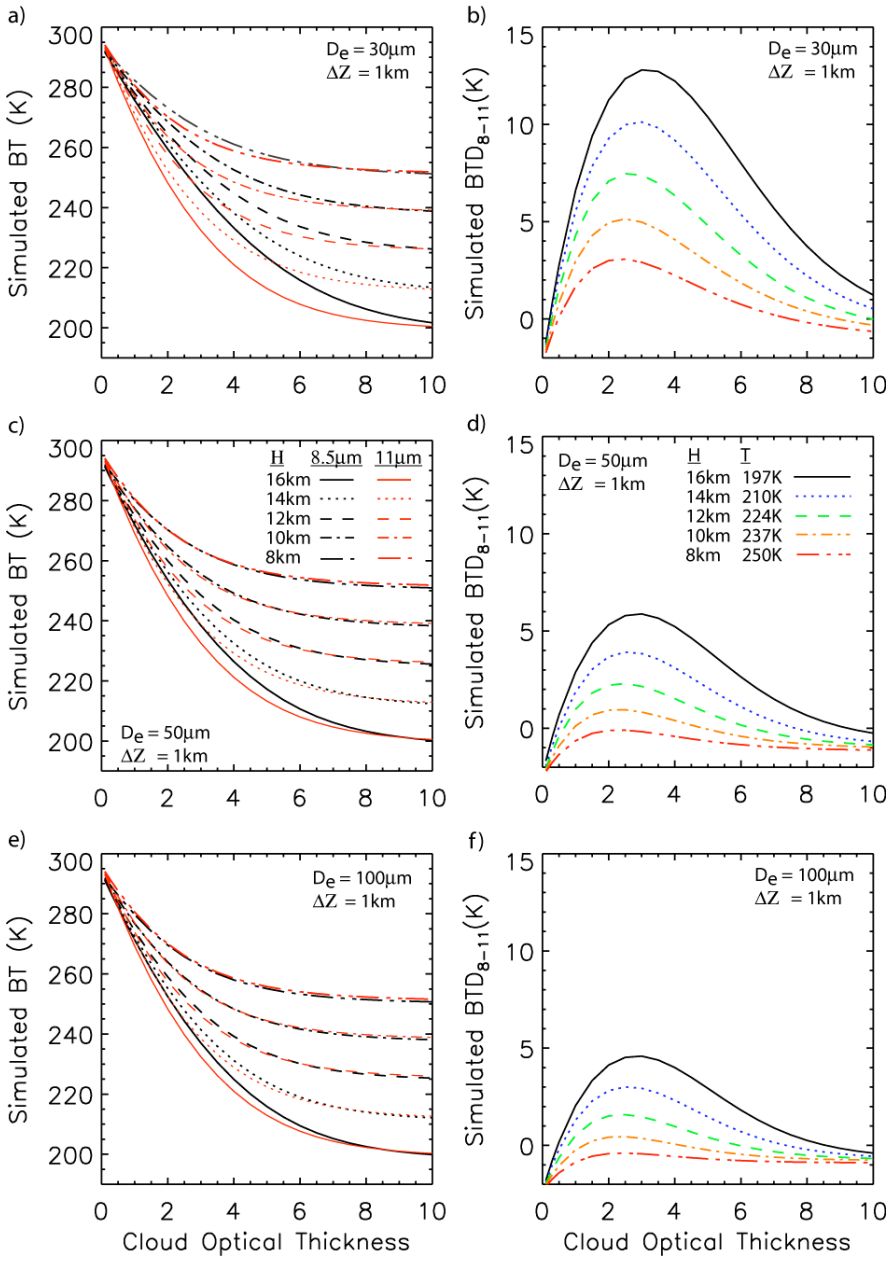

Fig. 14. Simulated brightness temperatures at 8.5 and 11.0 µm as a function of optical thickness, for clouds of varying height. Simulations are show for a), c), and e) clouds with effective diameters of 30, 50, and 100 µm, respectively, and b), d), and f) $BTD_{8.5\text{-}11.0}$ of corresponding left-panel plots.

cloud top becomes colder, the 11.0 μm brightness temperature decreases at a faster rate than the 8.5 μm brightness temperature, creating the larger $BTD_{8.5\text{-}11}$ for colder clouds. As the optical thickness becomes larger than ~3, the 8.5 μm absorption increases and begins to converge with the 11.0 μm BT. At around $\tau_{0.55} = 7$, saturation in the signal occurs and sensitivity to cloud properties is lost as the emissivity at each channel becomes similar.

We may conclude that the region of highest sensitivity for retrievals using the bi-spectral $BTD_{8.5\text{-}11}$ approach falls within an optical thickness range of $\tau_{0.55} = 2\text{-}6$, where $BTD_{8.5\text{-}11}$ is largest, but this range is narrowed as cloud temperature increases or as effective size increases. Clouds with cloud top temperatures colder than 224 K may be optimal for retrievals. For geometrically thicker clouds however, colder cloud tops may be required to maximize $BTD_{8.5\text{-}11}$ as transmission from warmer layers within the cloud becomes an increasingly important factor as discussed later in this study. It is clear that if we insert our cloud layer too high (cold) or too low (warm) in our model, we may retrieve very different results given the similar $BTD_{8.5\text{-}11}$ curves for clouds of differing cloud top temperatures and effective diameters. Error associated with the cloud top parameterization is investigated in Section 4.

3.3 Sensitivity to Cloud Layer Temperature

In this section, the sensitivity of simulated brightness temperatures at top-of-atmosphere to cloud geometric thickness is investigated. For a cloud with a fixed cloud

top height, extending the cloud base into lower (warmer) layers in the atmosphere changes the effective emitting temperature of the cloud. Prior results [11], [22] have shown that geometric thickness is an important cloud property that regulates the transmission of IR radiance through a cloud layer. By analyzing clouds with equivalent optical thickness, ice crystal effective size, and cloud top temperature, Chung *et al.* [11] and Hong *et al.* [22] show that IR brightness temperatures are colder for cloud layers with small temperature differences from cloud base to top (ΔT), or geometrically thin cloud, than for cloud layers for larger ΔT, or geometrically thick cloud. In this study, our model is used to simulate 8.5 and 11.0 μm BTs in the standard tropical atmosphere for clouds with geometric thicknesses of 0.5, 1, 2, 3 and 5 km (ΔT of 3.5, 6, 13, 20, and 32 K), optical thicknesses from 0.1 to 10, and cloud top heights of 12 and 15 km (224 and 204 K).

Figs. 15a, c, and e show the results for simulations of a cloud top at 12 km and effective diameters of 30, 50 and 100 μm, respectively, as a function of optical thickness. Each plotted line represents the BT of a cloud with a geometric thickness of 1, 2, 3, or 5 km minus the BT of a cloud with a thickness of 0.5 km (ΔZ BTD) at 8.5 μm (black) and 11.0 μm (red). The simulations show that as geometric thickness of a cloud layer increases and extends the cloud into warmer atmospheric layers, ΔZ BTD also increases, peaking at around 8 K for a 5 km thick cloud with optical thickness values of around 6 for 11.0 μm and an optical thickness of around 4 for 8.5 μm BTs. Physically, as a cloud layer extends into lower regions of the atmosphere, the effective emitting

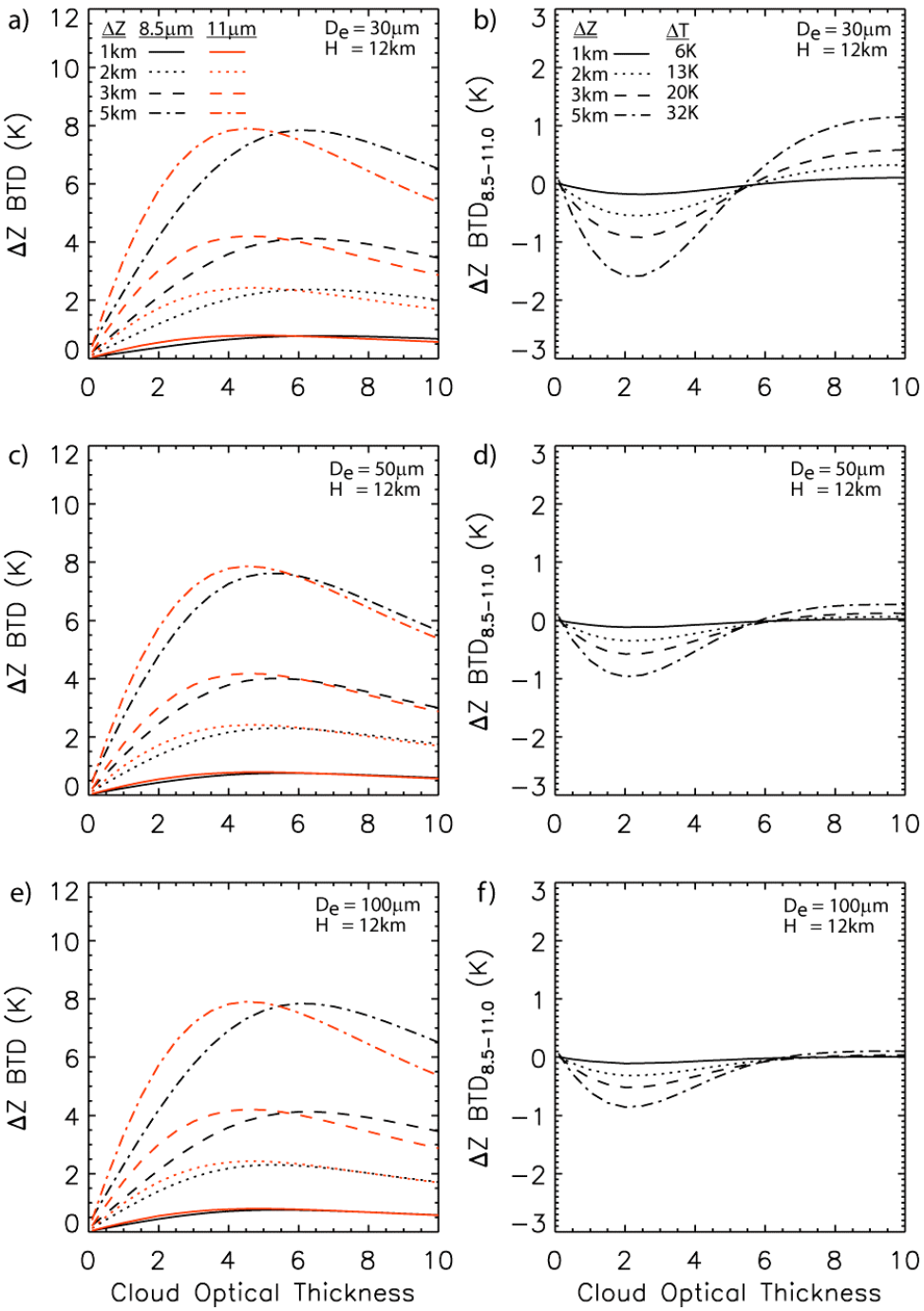

Fig. 15. Simulated 8.5 and 11.0 μm BTs for clouds with varying geometric thicknesses of 1, 2, 3, and 5 km minus BTs of a cloud with a fixed geometric thickness of 0.5 km as a function of optical thickness. Simulations are shown for a), c), e) clouds with an effective diameter of 30, 50 and 100 μm, respectively, and b), d), and f) $BTD_{8.5\text{-}11}$ from corresponding left-hand panels. Clouds have a fixed cloud top height of 12 km (224 K).

temperature at these wavelengths is warmer because of the absorption and emission by warmer ice crystals. Thus, BTs at 8.5 and 11.0 μm will be higher for a geometrically thick cloud when compared to a geometrically thinner cloud, with all other atmospheric parameters and cloud properties being equal.

Comparing the plots for different effective diameters, it is apparent that the cloud layer temperature difference is not only important for small ice crystals, but also for large ice crystals as ΔZ BTD is still as large as 8 K for a 5 km thick cloud with an effective diameter of 100 μm. The same may be stated for all optical thickness values between 0.2 and 10, where ΔZ BTD is still large for all values. It is important to note that even though sensitivity to cloud layer temperature still exists for large ice crystal sizes, and for very optically thin and thick clouds, it may still be difficult to infer cirrus cloud properties due to small $BTD_{8.5\text{-}11.0}$ in these regions.

If we consider geometric thickness in a cloud property retrieval using our $BTD_{8.5\text{-}11.0}$ approach, we may also be interested in the sensitivity of $BTD_{8.5\text{-}11.0}$ to changes in geometric thickness. Figs. 14b, d, and e show the ΔZ $BTD_{8.5\text{-}11}$ for each geometric thickness from a, c, and e respectively. Here, the $BTD_{8.5\text{-}11}$ for each thickness (1, 2, 3, and 5 km) is differenced from the 0.5 km $BTD_{8.5\text{-}11}$. In the plots, we can see as geometric thickness increases from 1 km to 5 km, ΔZ $BTD_{8.5\text{-}11}$ values increase from 0.5K to 1.5 K. The difference of $BTD_{8.5\text{-}11}$ for all thicknesses from that of a 0.5 km thick cloud peaks near an optical thickness of 2. As the effective diameter is increased, large ΔZ $BTD_{8.5\text{-}11}$ still exists, showing that geometric thickness may have a large influence on retrievals of clouds of all optical thicknesses and effective sizes.

A feature of note in the plots occurs at an optical thickness of 6.5, where the sign of ΔZ $BTD_{8.5\text{-}11}$ changes from negative to positive. At $\tau_{0.55} < 6.5$, $BTD_{8.5\text{-}11}$ for clouds of all geometric thicknesses is less than $BTD_{8.5\text{-}11}$ for a cloud with 0.5 km geometric thickness. For $\tau_{0.55} > 6.5$, the opposite is true. Analyzing the left-hand panels of Fig. 15, we can see that this is due to the 11.0 μm BT saturating at lower visible optical thickness values than the 8.5 μm BT due to higher absorption by ice crystals at this channel. This sign change is less drastic for larger effective diameters as the 8.5 μm absorption increases, but overall is not very significant itself in terms inferring cloud properties.

Fig. 16 is the same as Fig. 15, but for a cloud at a height of 15 km (204 K). For Figs. 16a, c, and e, there are still large differences in BTs between the various geometric thicknesses, and are comparable to the simulations at 12 km. Although the cloud top temperature is different in both simulations, ΔT remains the same for all geometric thicknesses except for at 5 km, where the 15 km high cloud is colder by 1 K. Analyzing the plots in Figs. 16b, d, and f, we see that ΔZ $BTD_{8.5\text{-}11}$ values are larger by roughly 0.2 - 0.5 K as compared to those in Fig. 15 for the lower (warmer) cloud top. This implies that for colder cloud tops, constraining the geometric thickness of the cloud becomes increasingly important for acquiring a more accurate retrieval.

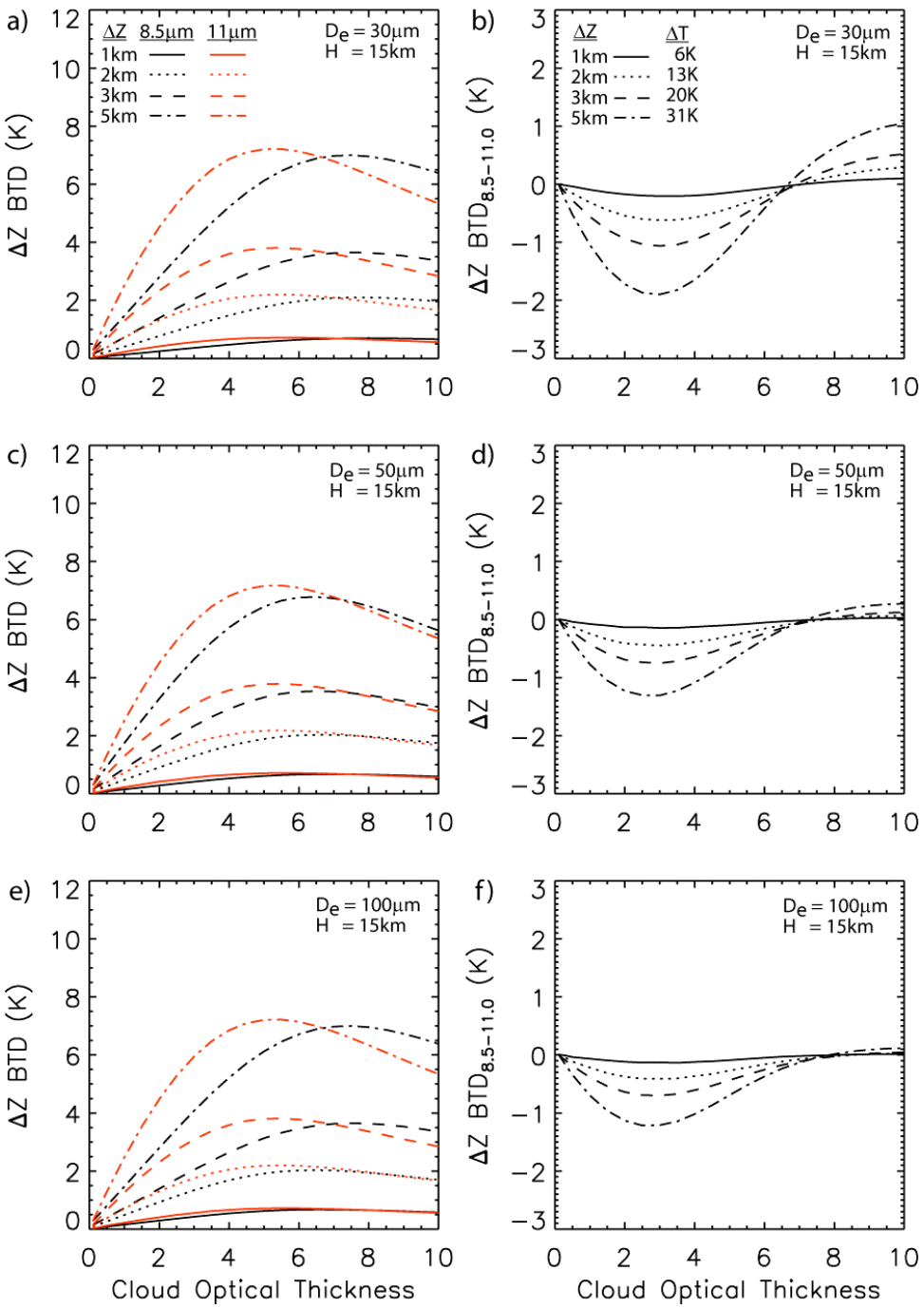

Fig. 16. Simulated 8.5 and 11.0 μm BTs for clouds with varying geometric thicknesses of 1, 2, 3, and 5 km minus BTs of a cloud with a fixed geometric thickness of 0.5 km as a function of optical thickness. Simulations are shown for a), c), e) clouds with an effective diameter of 30, 50 and 100 μm, respectively, and b), d), and f) $BTD_{8.5\text{-}11}$ from corresponding left-hand panels. Clouds have a fixed cloud top height of 15 km (204 K).

4. INFLUENCE OF CLOUD TEMPERATURE ON THE RETRIEVAL OF CIRRUS PROPERTIES

4.1 Methodology

After gaining an understanding of how cloud temperature, both as determined by both cloud height and cloud geometric thickness, influence simulated brightness temperatures at 8.5 and 11.0 μm, we now look to the retrieval of cirrus cloud effective particle size and optical thickness using Moderate Resolution Imaging Spectroradiometer (MODIS) IR observations. However, instead of using a standard tropical atmosphere, we use collocated Atmospheric Infrared Sounder (AIRS) retrievals of pressure, temperature, moisture and ozone profiles, as well as cloud top height. The correlated *k*-distribution method is used with the AIRS atmospheric profile retrievals to calculate clear-sky transmittances of the atmospheric layers, and the Baum v2 cirrus models developed for MODIS channels 29 and 31 are used for the bulk-scattering properties of ice crystals. Forward calculations are performed using the DISORT model, where simulated brightness temperatures (BTs) are computed for clouds with effective diameters between 10 and 120 μm, and optical thickness between 0 and 30. The simulations are then used to construct lookup tables, which are interpolated to finer resolution. Finally, MODIS observed 8.5 and 11.0 μm BTs are then used to retrieve effective diameter and optical thickness values from the lookup tables.

A daytime scene from MODIS, of single-layer cirrus over a tropical ocean, is chosen. Retrievals are performed for clouds of varying cloud top heights and geometric thicknesses, and the results are analyzed and compared to the MODIS level-2 standard retrieval product.

4.2 Instruments and Data

On May 4th, 2002, the National Aeronautics and Space Administration (NASA) launched the Aqua satellite as part of the Earth Observing System (EOS) and "A-train" constellation. The Aqua satellite maintains two instruments used in our study, the Moderate Resolution Imaging Spectroradiometer (MODIS) and the Atmospheric Infrared Sounder (AIRS). EOS-Aqua is a sun-synchronous polar-orbiting satellite at an altitude of 705 km and can attain global coverage in less than two days.

MODIS is an infrared spectrometer with 36 channels. The spectral coverage is between 0.415 and 14.235 μm with varying spatial resolution of 250 m, 500 m, and 1000m and scans across a swath-width of 2330 km [36]. To ensure that only MODIS pixels which contain cirrus clouds are used in the retrieval, the MODIS cloud mask [32] and phase discrimination [12] flags are checked. Only pixels flagged as "confident cloudy" are chosen and further filtering occurs by checking the 1 km Quality Assurance and selecting only those flagged as "ice."

To perform the retrievals in this study, the MODIS level 1b calibrated radiance product (MYD021KM) is used in the selected scene for channels 29 and 31, which are then converted to brightness temperatures using the Planck function. The results of the

retrieval are then compared to the MODIS level-2 cloud product (MYD06) effective size and optical thickness, which uses solar/NIR reflectance data [31]. All products used were processed using the MODIS collection 5 processing algorithm.

The AIRS instrument is a continuously operating, cross-track hyperspectral IR sounder consisting of a telescope which feeds an echelle spectrometer. The spectrometer analyzes IR radiation at 2378 channels between 3.74-4.61 μm, 6.20-8.22 μm, and 8.80-15.4 μm with a spectral resolution of $\lambda/\lambda\Delta = 1200$ [2]. A scan mirror on the instrument scans on 49.5° either side of nadir with a swath width of 1650 km and a spatial resolution of 13.5 km at nadir. Each scan line contains 90 AIRS footprints and is repeated every 8/3 seconds, including four views for calibration.

The AIRS version 4, level-2 standard retrieval [1] product provides atmospheric temperature, pressure, ozone, and moisture profiles for 28 atmospheric levels, as wells as for cloud top height which is derived using the CO_2 slicing technique [8], [40] and surface skin temperature. These surface and atmospheric parameters are retrieved at a spatial resolution of 45 km x 45 km, therefore several MODIS pixels may be present within one AIRS pixel requiring collocation of the datasets. To gain better control over cloud top placement and geometric thickness, the vertical spatial resolution of the atmospheric profile must be increased. To do this, the atmospheric profile at 5 AIRS levels between 100 hPa and 300 hPa, where cirrus clouds are likely to occur, are linearly interpolated to 20 levels. Retrievals may then be performed with the cloud placed at any desired layer.

4.3 Retrievals with Varying Cloud Top Height

For the retrieval of cirrus clouds with varying cloud top height (temperature), a MODIS daytime granule is chosen which exhibits a case of a single-layer, homogeneous cirrus cloud over the tropical Pacific Ocean (Fig. 17). Although the IR-based retrieval was developed for nighttime retrievals, we choose a daytime case for this study where operational retrievals can be used for comparison purposes. Figs. 18a and b show corresponding plots for MODIS level-2 retrieved optical thickness and effective radius, respectively, for the case area. The MODIS optical thickness range falls within our most sensitive region to cloud top height from the theoretical simulations in Section 3.2, where $BTD_{8.5\text{-}11}$ is largest, for $\tau_{0.55}$ between 2 and 6. The MODIS effective radius is generally below 30 μm, which is on the threshold of low-to-moderate sensitivity. Based on the MODIS product, $BT_{8.5\text{-}11}$ should have adequate sensitivity to retrieve cirrus properties.

Two collocated AIRS profiles are used for atmospheric profile data, as well as for cloud top height from the AIRS derived cloud top pressure (CTP). Fig. 18c shows the coverage of AIRS pixels in the case area indexed as numbers 549 and 500, overlapping approximately 1100 MODIS pixels. Since the AIRS CTP usually places the cloud top between two AIRS levels, the atmosphere between 100 hPa and 300 hPa is interpolated from 5 to 20 atmospheric levels. With the finer vertical resolution in the profile, cloud properties are retrieved for three cloud top heights. The first retrieval places the cloud at the AIRS specified cloud top height. The derived CTP for pixels 549 and 550 are 126 hPa and 148 hPa respectively. The second and third retrievals place the cloud top at the

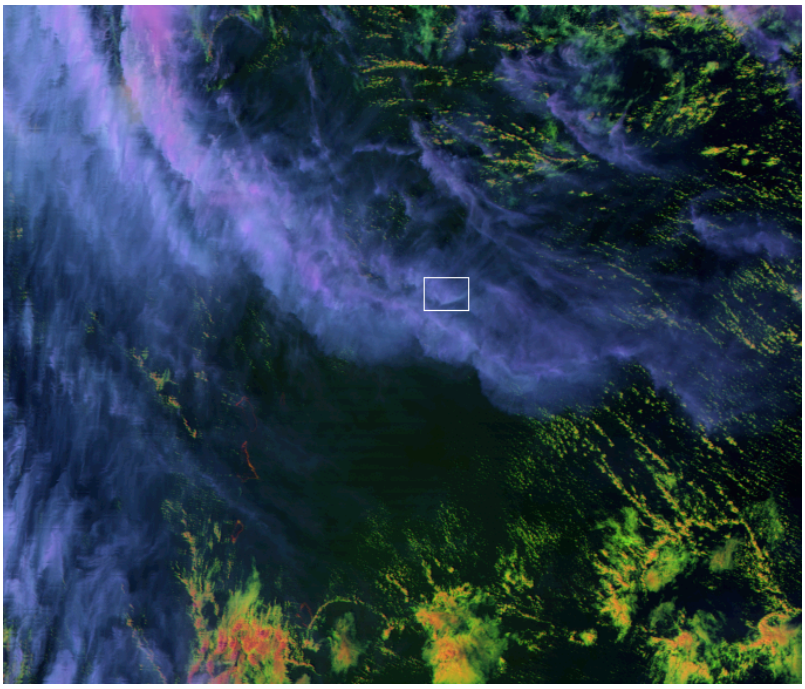

Fig. 17. a) False color image of MODIS case area from granule MYD021KM.A2005354.0140 (0.65 µm in red, 2.13 µm in green, and 11.0 µm in blue), approximately ~1100 pixels.

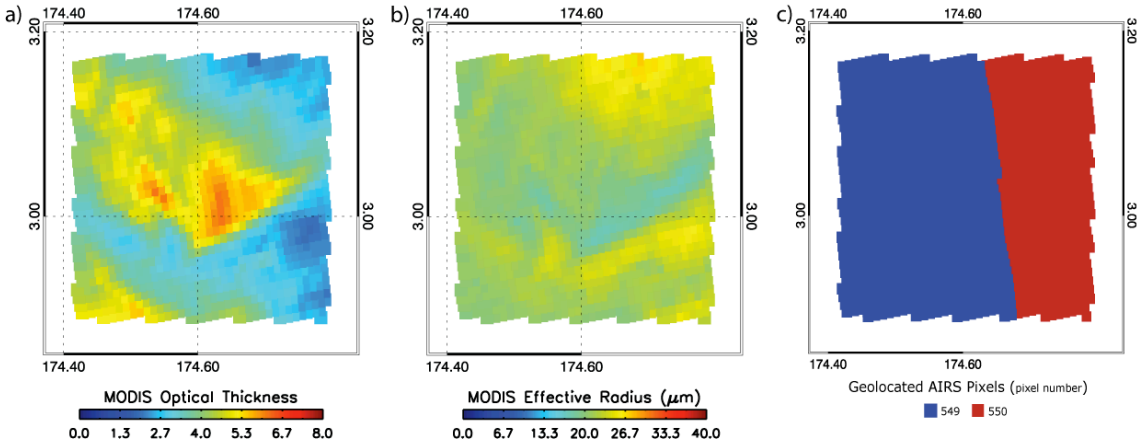

Fig. 18. a) MODIS retrieved cloud optical thickness, b) MODIS retrieved effective radius and c) collocated AIRS pixels within the scene.

next highest and next lowest AIRS levels (100 hPa and 150 hPa, respectively) from the original 28 AIRS output levels, to examine the influence of changes in cloud top temperature to the retrieval results. The cloud layer thickness for each case is fixed at 1 km.

Because IR radiances are sensitive to atmospheric profile and cloud top temperature, simulations must be performed and lookup tables constructed for each AIRS profile and cloud top temperature assumed. Fig. 19 shows the IR bi-spectral plots representing the lookup tables for each retrieval case, which result from simulating IR brightness temperatures with the data from AIRS pixels 549 and 550 at three different cloud top temperatures. The IR observations from each MODIS pixel are also plotted on the figures. Plotted lines on the right-hand side of the figures, where optical thicknesses are small, vary little between the simulations for each cloud top. These regions are strongly dependent on the surface skin temperature and background atmospheric profile, whose emission is mostly transmitted through optically thin cloud. Even between pixels 549 and 550, where differences in these parameters differ slightly, no strong influence can be seen in the bi-spectral plots (Table 2). Analyzing retrievals from each AIRS pixel separately did not show that one pixel performed better than the other when compared to MODIS operational cloud product. This could be due to the fact that for moderately optically thick clouds such as in this case, the retrievals may be more sensitive to cloud top height than to the atmospheric profile or skin temperature, similar to Huang *et al.* [24].

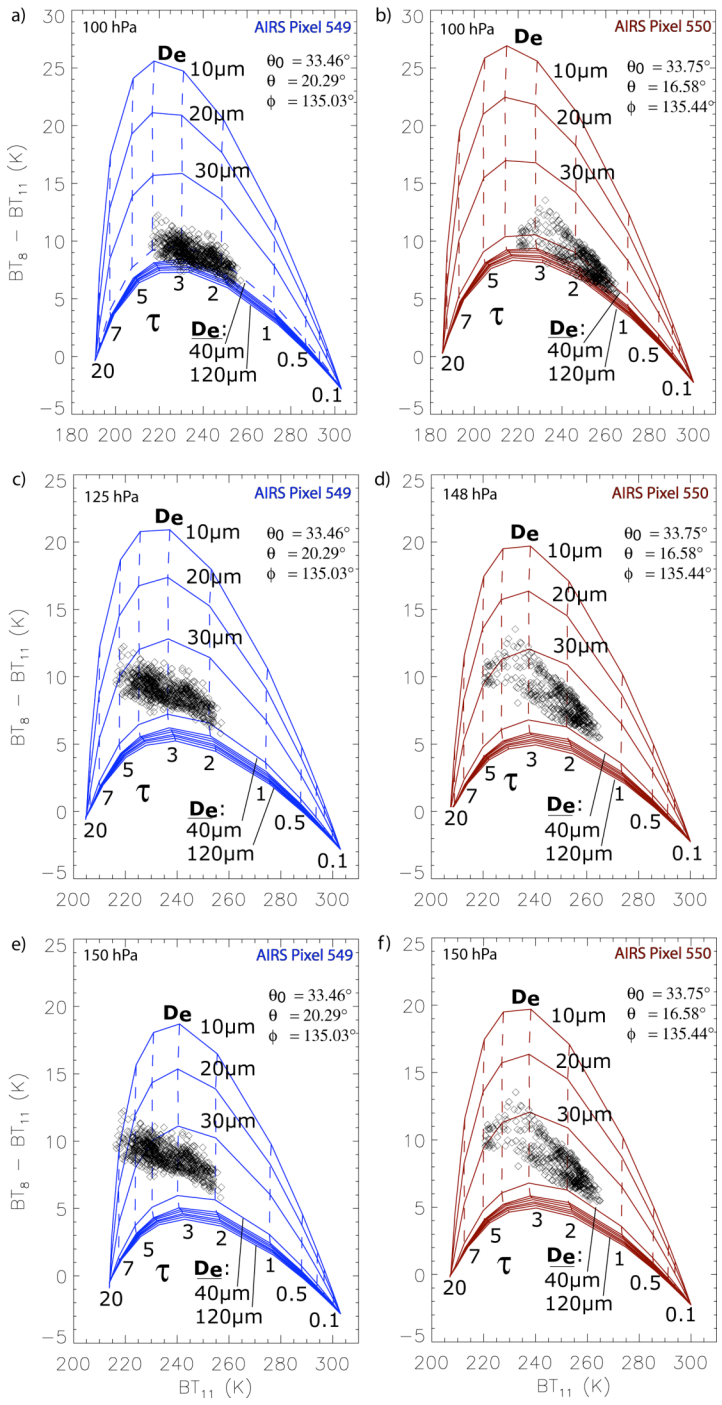

Fig. 19. IR bi-spectral plots for clouds with varying height. Plots are shown for a), b), AIRS pixels 549 (blue) and 550 (red) at the AIRS 100 hPa pressure level, c), d), at the AIRS derived cloud top pressure level, and e), f), at the AIRS 150 hPa pressure level. Cloud geometric thickness is fixed at 1km. MODIS IR observations are overplotted.

Table 2. Cloud and profile data for three retrievals with varied cloud top height.

AIRS Pixel	Cloud Top Pressure (hPa)	Cloud Top Temp (K)	Cloud Base Temp (K)	Height (km)	Skin Temp (K)
549	100	188.7	198.4	16.6	306
550	100	184.5	193.2	16.6	313
549	127.5	203	213	15.2	306
550	150	206	217	14.3	313
549	150	212.8	217	14.2	306
550	150	206	217	14.3	313

On the other hand, plotted lines in regions of higher optical thickness values show significant differences between the simulations with cloud tops of ~185 K and 213 K. Comparing Figs. 19a and e, as the cloud top temperature is warmed, the left edge of the plot is shifted to the right to the minimum 11.0 μm BT close to the assumed cloud top temperature. Here we see the effects of strong absorption at this channel where cloud top temperature has a strong influence on the effective emitted temperature.

In regions of the plots for moderate optical thickness values ($1 < \tau_{0.55} < 7$), the effect on the 8.5 and 11.0 μm BTs from warming the cloud top temperature is shown. In Fig. 19a, the maximum $BTD_{8.5\text{-}11}$ for a cloud with an effective diameter of 10μm and cloud top temperature of 185 K is ~25 K. For a similar cloud with a cloud top temperature of 212 K, the maximum $BTD_{8.5\text{-}11}$ is decreased to about 18 K. This is an expected result indicated by our theoretical study in Section 3.2, where maximum $BTD_{8.5\text{-}11}$ values also decreased with increasing cloud top temperature. The effect on the

.

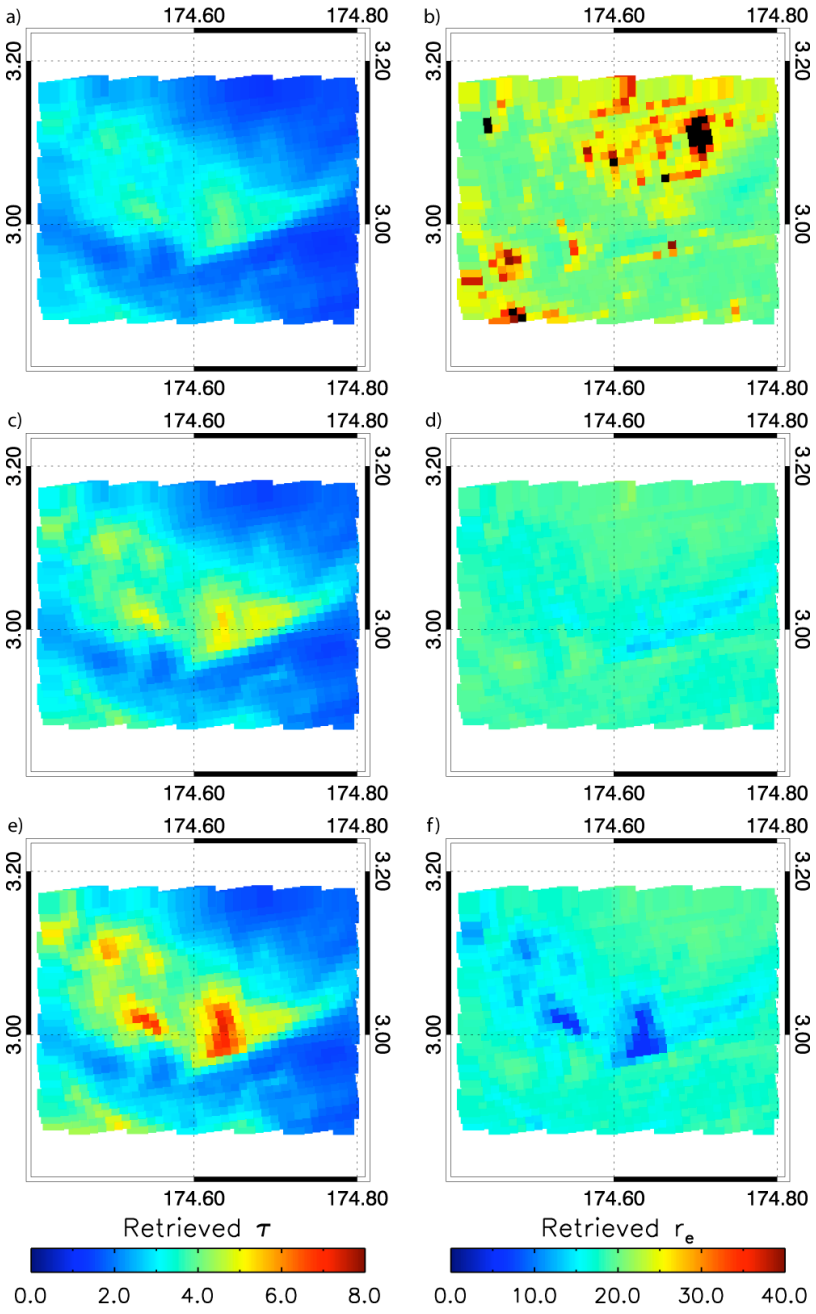

Fig. 20. Geolocated retrieved optical thickness and effective radius of case area for varying cloud height. Plots shown for a), b), a cloud at the AIRS 100 hPa pressure level, c), d), at the AIRS derived cloud top pressure level, and e), f), at the AIRS 150 hPa pressure level.

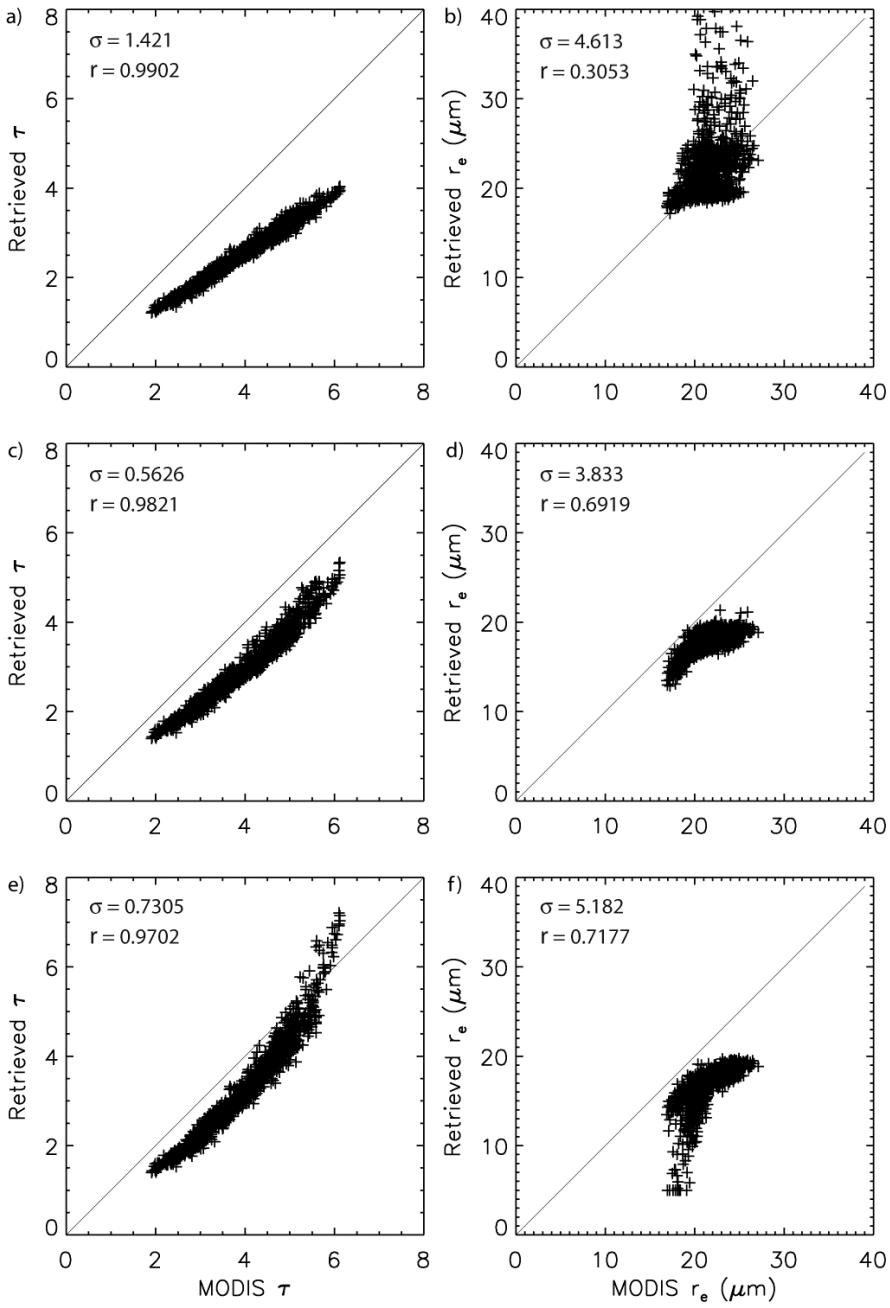

Fig. 21. Scatter plots comparing retrieved values of optical thickness and effective radius to MODIS MOD06 retrieved values corresponding to the plots in Fig. 20.

retrieval can be seen plainly, as the MODIS IR observations are overplotted on a different portion of the bi-spectral plot between Figs. 19a and e. The same relationship is noted for AIRS pixel 550 in Figs. 18b, d, and f, where $BTD_{8.5\text{-}11}$ also decreases with increasing cloud top temperature.

Fig. 20 shows geolocated results of the retrievals for optical thickness and effective size, with corresponding scatter plots in Fig. 21. The scatter plots compare the retrieved cirrus properties to those of the MODIS level-2 cloud product, which we will assume to be truth. At 100 hPa, the optical thickness underestimates MODIS suggesting the simulated 11 μm BT is too cold. Optical thickness retrievals perform better for the cases with warmer cloud tops, although they slightly underestimate MODIS. Statistically, the optical thickness retrievals perform well in each case, although the standard deviations are smaller for the retrievals of warmer clouds, around 0.6.

Evaluating results for effective size, we can see the influence of the colder cloud top from our theoretical study where $BTD_{8.5\text{-}11}$ had much higher maximums than for warm clouds. Although many retrieved pixels lay close to the 1-to-1 line with the MODIS retrieved effective size in the 100 hPa case, several pixels sporadically overestimate MODIS. These pixels correspond to the MODIS IR observations overplotted in the region of little sensitivity to effective size in the bi-spectral plots. Again, as cloud top temperatures become warmer, the MODIS IR observations allow for a more consistent retrieval of effective size. Here, the correlation coefficient, r, increases from 0.3 to 0.71 in the 150 hPa cloud retrieval. However, compared to the MODIS retrieval, the effective size is still largely underestimated for the most optically

thick cloud. Here we may see a slight bias due to the cloud top temperature in AIRS pixel 549 being too warm, resulting in a large shift of the bi-spectral plot to the right, and causing the MODIS observations to be plotted at very large optical thickness, and very small effective diameters. Validation of cloud top height to determine the actual cloud top temperature is required to gain the necessary confidence in IR retrievals.

4.4 Retrievals with Varying Geometric Thickness

We now perform another series of retrievals for effective size and optical thickness within our case area. Instead of altering the cloud top height, we use the AIRS derived CTP as a fixed cloud height, and vary the cloud geometric thickness. Retrievals are performed for cloud geometric thicknesses of 1, 3, and 5 km. Again, the AIRS atmospheric profile has been interpolated to achieve finer vertical resolution. Table 3 shows the atmospheric and cloud properties for each AIRS pixel and retrieval case, along with the temperature difference, ΔT, between the cloud base and top. For a thickness of 1 km, ΔT equals ~10K for each pixel; for a thickness of 3 km, ΔT equals 18.5 and 30 K for pixel 549 and 550, respectively; and for the 5 km thick cloud, ΔT equals 32.7 and 38.7 K for each pixel, respectively.

Fig. 22 shows the IR bi-spectral plots which represent the lookup tables for each retrieval case with varying cloud geometric thickness. Fig. 22a and b are of a 1 km thick cloud, c and d of a 3 km thick cloud, and e and f of a 5 km thick cloud for each AIRS pixel. Comparing the figures for each individual retrieval case, the plots only shift slightly left and right between AIRS pixels 549 and 550, due to the few Kelvin

Table 3. Cloud and profile data for three retrievals with varied cloud geometric thickness.

AIRS Pixel	Cloud Top Temp (K)	Cloud Base Temp (K)	Skin Temp (K)	ΔT (K)	ΔZ (km)
549	203	213	306	10	1
550	206	217	313	11	1
549	203	221.5	306	18.5	3.1
550	206	236	313	30	3.1
549	203	235.7	306	32.7	5
550	206	244.7	313	38.7	4.6

differences in cloud top temperature and skin temperature. However, comparing the 3 km plots (Figs. 22c, d) where ΔT is ~12 K between AIRS pixels 549 and 550, we begin to see the effects of extending the cloud base into warmer regions of the atmosphere. The main impact is that the maximum $BTD_{8.5\text{-}11}$ is decreased with increasing thickness, much like the previous case of warming the cloud top temperature. Between the cases of varying geometric thickness, the same effect on $BTD_{8.5\text{-}11}$ is seen for increasing ΔT. For the 1km case, the maximum $BTD_{8.5\text{-}11}$ is close to 21 K and 20 K for pixels 549 and 550, respectively. In the 5 km case, these values are decreased to 18 K and 16 K, respectively. The result is mainly due to the bi-spectral plots shifting down, but also narrowing between the minimum and maximum $BTD_{8.5\text{-}11}$ values along the plotted lines of effective diameter. Physically, as a cloud extends into warmer layers of the atmosphere, the 11.0 μm brightness temperature becomes warmer due to ice crystals at warmer temperatures. Since the 8.5 μm radiance is not as strongly absorbed, it is less

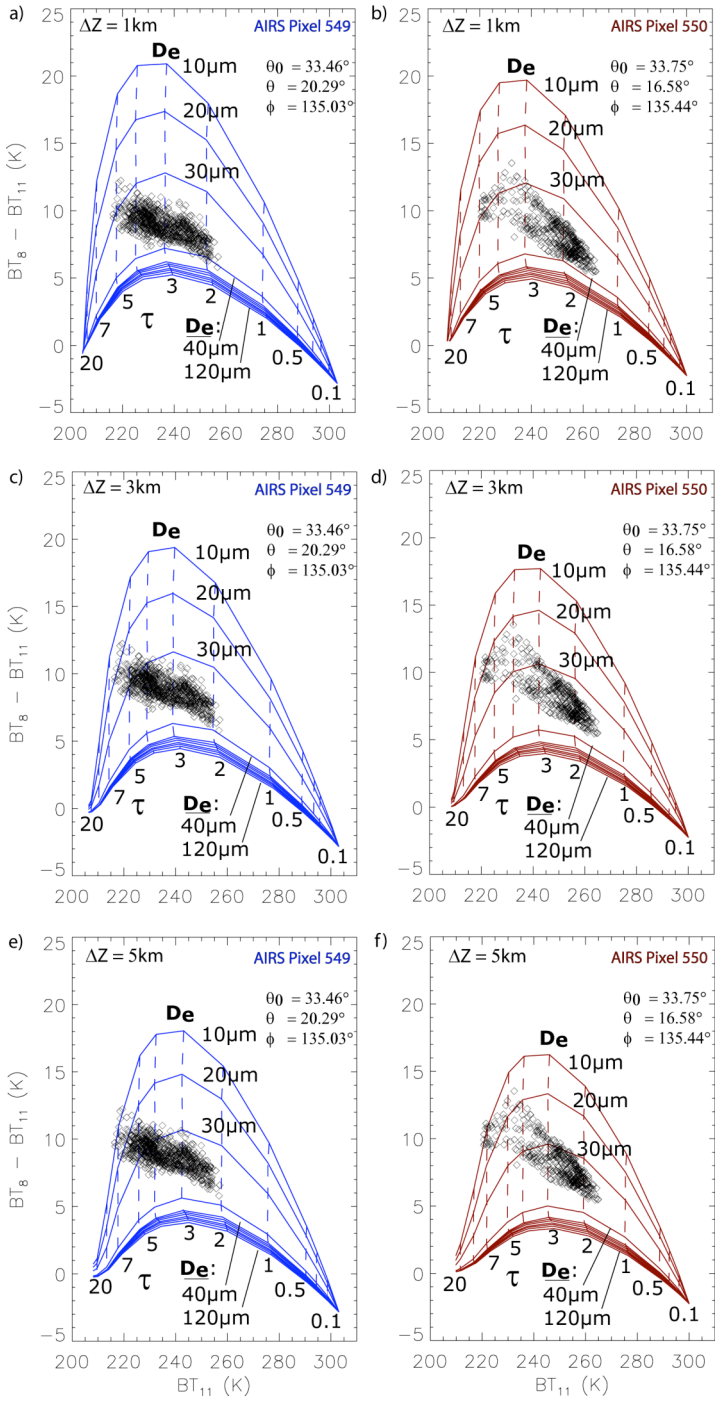

Fig. 22. IR bi-spectral plots for a cloud at the AIRS derived cloud top pressure level with varying geometric thickness. Plots shown for a), b) AIRS pixels 549 and 550, respectively, for a 1km thick cloud, c), d) for a 3km thick cloud and e), f) for a 5km thick cloud. MODIS IR observations are overplotted.

sensitive to the cloud layer temperature and $BTD_{8.5\text{-}11}$ values therefore decrease with increasing ΔT.

Fig. 23 shows the geolocated results for each retrieval case along with corresponding scatter plots in Fig. 24. Optical thickness retrievals are fairly consistent among each case, and compare well with the MODIS retrievals. For the 1 km retrieval, retrieved optical thickness underestimates MODIS, but has very high correlation. As the cloud layer thickens, the optical thickness retrieval values increase, but then begin to overestimate MODIS in the most optically thick regions.

Effective size retrievals also underestimate MODIS, with sensitivity to changes in geometric thickness. As geometric thickness increases to 5 km, very small particle sizes are retrieved where the optical thickness is overestimated. In the effective size retrievals, there is not much improvement as shown by the correlation coefficient, increasing only from 0.69 to 0.71 when ΔT increases from 10 K to ~32-38 K. However, the standard deviation drastically increases when the cloud is geometrically thicker, denoting more error in the retrieval results.

From each case with varied cloud top height or geometric thickness, we see that warming the cloud layer has a profound effect on the retrieval of cirrus cloud effective size and optical thickness. After analysis of the bi-spectral plots and results compared to MODIS (if taken as truth), one may argue that in this case study, the actual cloud top height is higher than the AIRS derived level, and that the cloud is thicker than 1km. This seems plausible, since for warmer cloud tops, the bi-spectral plots were shifted too

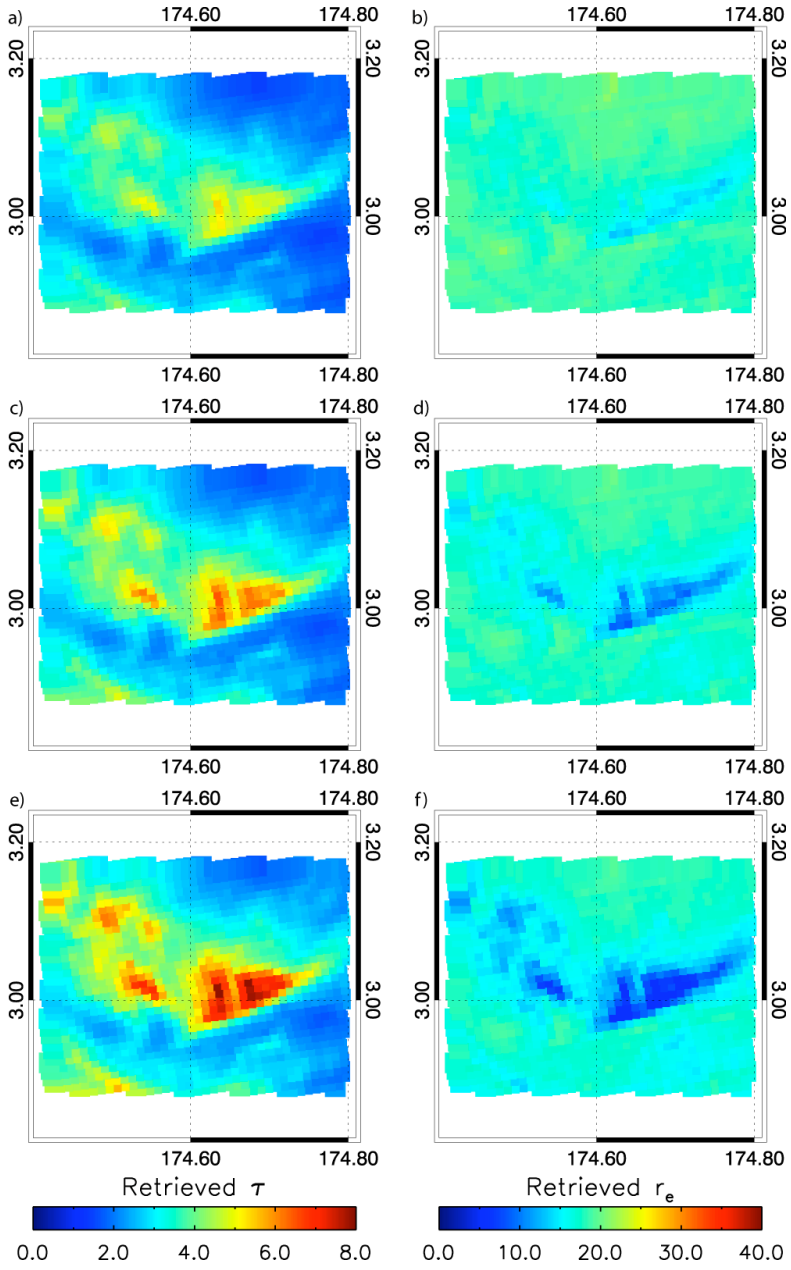

Fig. 23. Geolocated retrieved optical thickness and effective radius of case area for a cloud at the AIRS derived cloud top pressure level and varying geometric thickness. Plots shown for a), b) a cloud with 1 km thickness, c), d) a cloud with 3 km thickness, and e), f) a cloud with 5 km thickness.

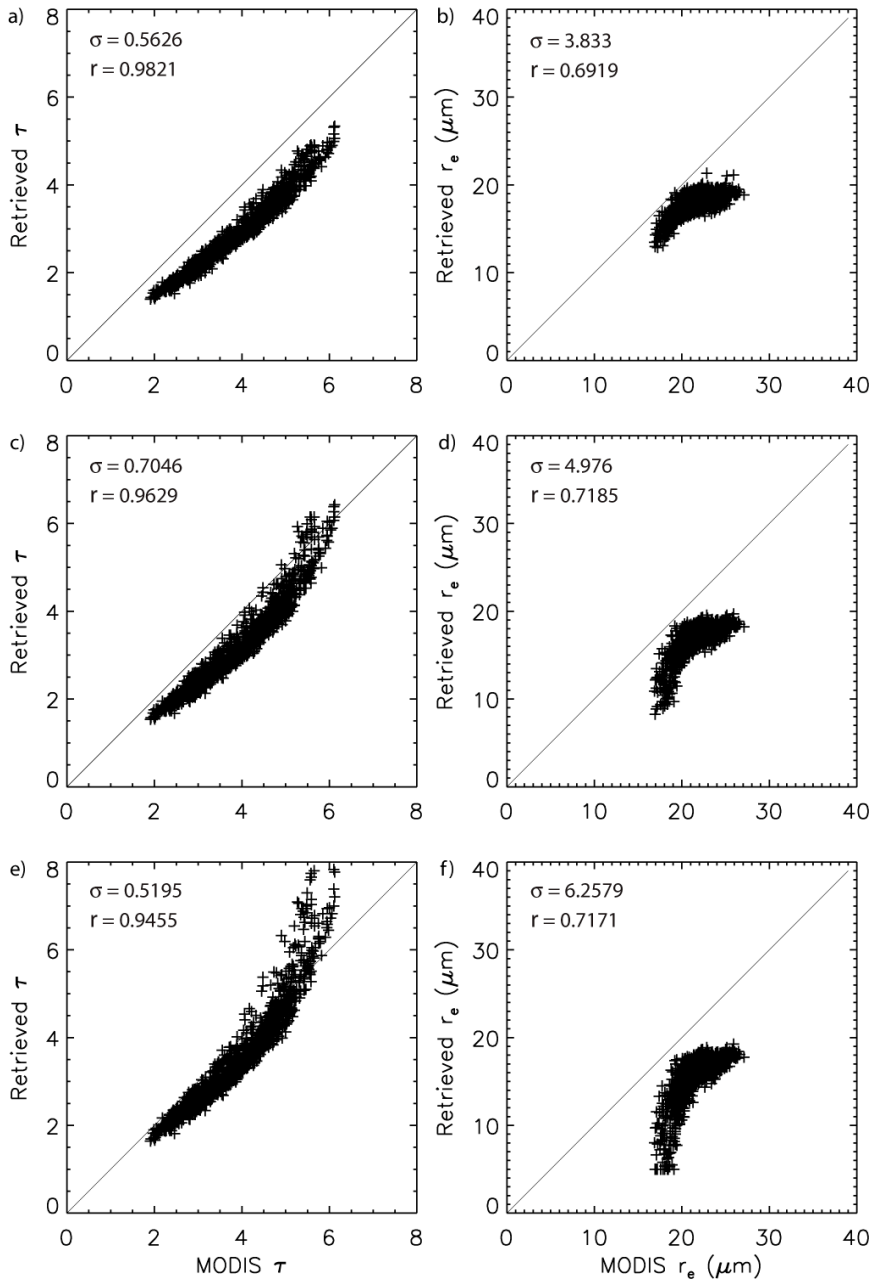

Fig. 24. Scatter plots comparing retrieved values of optical thickness and effective radius to MODIS MOD06 retrieved values corresponding to the plots in Fig. 23.

far to the right, especially in AIRS pixel 549. As the optical thickness and effective size values fall within the region of highest sensitivity of $BTD_{8.5\text{-}11.0}$ to cloud top height and geometric thickness as shown in Section 3, the importance of accurately placing a cirrus cloud in the atmosphere has been demonstrated. Validation of these parameters is thus a requirement to improve the results produced with our retrieval model.

5. DISCUSSION AND SUMMARY

The first part of this thesis has focused on the computation of ice crystal bulk-scattering properties to create cirrus cloud models for use with the Infrared Atmospheric Sounding Interferometer (IASI) onboard the METOP-A satellite. The creation of these models was based on the single-scattering database developed by Yang *et al.* [56] for six individual ice crystal habits, and followed the process of Baum *et al.* [4], [6], [7] closely. Cirrus models for the six individual ice crystals, as well as for one habit distribution were then used to simulate brightness temperatures in the IASI spectrum using the discrete ordinates radiative transfer (DISORT) model. The simulations showed that regions of the spectrum, particular in window channels between 790 and 1200 cm^{-1}, were strongly dependent on the assumed habit distribution and cirrus model used. Comparisons of brightness temperatures simulated with the each cirrus model showed differences on the order of 2 – 8 K, which could have significant effects if IASI measurements were used for cirrus cloud property retrievals.

The second part of this study focused on the sensitivity of simulated brightness temperatures at 8.5 and 11.0 μm to cloud temperature. A model was developed based on DISORT to simulate clouds at varying heights and geometric thicknesses in a standard tropical atmosphere. For clouds with visible optical thicknesses between 2 and 6, and with effective diameters less than 50 μm, it was shown that varying the cloud top temperature from 197K to 250 K decreased the 8.5-11.0 μm brightness temperature

difference ($BTD_{8.5\text{-}11.0}$) from 14 K to just 3 K. Changes in geometric thickness from 0.5 km to 5 km for a cloud with a fixed height decreased ΔZ $BTD_{8.5\text{-}11.0}$ upwards of 2 K. From these results, it can be expected that error in cloud top temperature and cloud layer temperature could significantly impact the retrieval of cirrus cloud properties using the $BTD_{8.5\text{-}11.0}$ approach.

To assess this impact, the model was applied to a retrieval of cirrus cloud effective size and optical thickness for a MODIS scene containing single-layer cirrus cloud over a tropical ocean surface. In the model, AIRS standard retrieval profiles for 28 atmospheric levels were interpolated to finer vertical resolution, and 8.5 and 11.0 μm brightness temperatures were simulated for clouds of varying height and geometric thickness. MODIS IR observations at these channels were then used to infer cirrus properties from lookup tables based on the $BTD_{8.5\text{-}11.0}$ approach. The bi-spectral plots representing the lookup tables showed considerable differences when cloud top temperature was increased by 20 K, or when the cloud layer was extended into warmer regions of the atmosphere by increasing the geometric thickness. By warming the cloud layer, 11.0μm BTs were also warmed, decreasing maximum $BTD_{8.5\text{-}11.0}$. The influence on the retrieval was to increase the retrieved optical thickness and decrease the effective size. However, by warming the cloud layer, improvements were shown in the retrieval results when compared to MODIS retrieval products.

The investigation has shown that cloud top height (temperature) and geometric thickness are an important parameterization in the $BTD_{8.5\text{-}11.0}$ bi-spectral retrieval approach. Validation of these cloud properties is needed to increase confidence in any

results. It is important, however, to realize the limitations of using this two-channel retrieval to infer cirrus cloud properties in the IR spectrum. Because of the sensitivities of IR brightness temperatures, not only to cloud properties, but also to the noise contributed by the background surface and atmosphere, more robust techniques may be required to achieve valid nighttime retrievals of cirrus cloud optical thickness and effective size. The use of hyperspectral measurements from instruments such as IASI may be a useful tool to reach this goal.

REFERENCES

[1] "AIRS Level-2 Algorithm Theoretical Basis Document," NASA, Pasadena, CA, 2001.

[2] H. H. Aumann, M. T. Chahine, C. Gautier, M. D. Goldberg, E. Kalnay, L. M. McMillin, H. Revercomb, P. W. Rosenkranz, W. L. Smith, D. H. Staelin, L. L. Strow, and J. Susskin, "AIRS/AMSU/HSB on the Aqua mission: Design, science objectives, data products, and processing systems," *IEEE Trans. Geosci. Remote Sens.*, vol. 41, pp. 253-264, 2003.

[3] R. J. Bantages, J. E. Russel, and J. D. Haigh, "Cirrus cloud top-of-atmosphere spectra in the thermal infrared," *J. Quant. Spectrosc. Radiat. Transf.*, vol. 63, pp. 487-498, 1999.

[4] B. A. Baum, A. J. Heymsfield, P. Yang, and S. T. Bedka, "Bulk scattering properties for the remote sensing of ice clouds. Part I: Microphysical data and models," *J. Appl. Meteorol.*, vol. 44, pp. 1885-1895, 2005.

[5] B. A. Baum, D. P. Kratz, P. Yang, S. C. Ou, Y.-X. Hu, P. F. Soulen, and S.-C. Tsay, "Remote sensing of cloud properties using MODIS airborne simulator imagery during SUCCESS 1. Data and models," *J. Geophys. Res*., vol. 105, pp. 11, 767-11780, 2000.

[6] B. A. Baum, P. Yang, A. J. Heymsfield, S. Platnick, M. D. King, Y.-X. Hu, and S. T Bedka, "Bulk scattering properties for the remote sensing of ice clouds. Part II: Narrowband models," *J. Appl. Meteorol.*, vol. 44, pp. 1896-1911, 2005.

[7] B. A. Baum, P. Yang, S. L. Nasiri, A. K. Heidinger, A. J. Heymsfield, and J. Li, "Bulk scattering properties for the remote sensing of ice clouds. Part 3: High resolution spectral models from 100 to 3250 cm^{-1}," *J. Appl. Meteor. Clim*., vol. 46, pp. 423-434, 2005.

[8] M. T. Chahine, "Remote sounding of cloud atmospheres. I. The single cloud layer," *J. Atmos. Sci*., vol. 31, pp. 233-243, 1974.

[9] H. Chepfer, P. Goloub, J. Spinhirne, P. H. Flamant, M. Lavorato, L. Sauvage, G. Brogniez, and J. Pelon, "Cirrus cloud properties derived from POLDER-1/ADEOS polarized radiances: First validation using ground-based lidar network," *J. Appl. Meteorol*., vol. 39, pp. 154-168, 2000.

[10] M. Chiriaco, H. Chepfer, V. Noel, A. Delaval, M. Haeffelin, P. Dubuisson, and P. Yang, "Improving retrievals of cirrus cloud particle size coupling lidar and three-channel radiometric techniques," *Mon. Wea. Rev*., vol. 132, pp. 1684-1700, 2004.

[11] S. Chung, S. Ackerman, P. F. Van Delst, and W. P. Menzel, "Model calculations and interferometer measurements of ice-cloud characteristics," *J. Appl. Meteorol.*, vol. 39, pp. 634-644, 2000.

[12] "Cloud Top Properties and Cloud Phase Algorithm Theoretical Basis Document," NASA, Greenbelt, MD, 2002.

[13] J. S. Foot, "Some observations of the optical properties of clouds: II Cirrus," *Quart. J. Roy. Meteorol. Soc.*, vol. 114, pp. 145-164, 1988.

[14] P. N. Francis, A. Jones, R. W. Saunders, K. P. Shine, A. Slingo, and Z. Sun, "An observational and theoretical study of the radiative properties of cirrus: Some results from ICE'89," *Quart. J. Roy. Meteorol. Soc.*, vol. 120, pp. 809-848, 1994.

[15] Q. Fu and K. N. Liou, "On the correlated *k*-distribution method for radiative transfer in nonhomogeneous atmospheres," *J. Atmos. Sci*., vol. 49, pp. 2139-2156, 1992.

[16] Q. Fu, W. B. Sun, and P. Yang, "On modeling of scattering and absorption by cirrus nonspherical ice particles at thermal infrared wavelengths," *J. Atmos. Sci.*, vol. 56, pp. 2937-2947, 1999.

[17] Q. Fu, P. Yang, and W. B. Sun, "An accurate parameterization of the infrared radiative properties of cirrus clouds for climate models," *J. of Climate*, vol. 25, pp. 2223-2237, 1998.

[18] B.-C. Gao, P. Yang, W. Han, R.-R. Li, and W.J. Wiscombe, "An algorithm using visible and 1.38-μm channels to retrieve cirrus cloud reflectances from aircraft and satellite data," *IEEE Trans. Geosci. Remote Sens*., vol. 40, pp. 1659-1688, 2002.

[19] A. J. Heymsfield, A. Bansemer, P. R. Field, S. L. Durden, J. Stith, J. E. Dye, W. Hall, and T. Grainger, "Observations and parameterizations of particle size distributions in deep tropical cirrus and stratiform precipitating clouds: Results from in situ observations in TRMM field campaigns," *J. Atmos. Sci.*, vol 59, pp. 3457-3491, 2002.

[20] A. J. Heymsfield, S. Matrosov, and B. A. Baum, "Ice water path-optical depth relationships for cirrus and precipitating cloud layers," *J. Appl. Meteorol.*, vol. 42, pp. 1369-1390, 2003.

[21] A. J. Heymsfield, and L. M. Miloshevich, "Parameterizations for the cross-sectional area and extinction of cirrus and stratiform ice cloud particles," *J. Atmos. Sci.*, vol. 60, pp. 936-956, 2003.

[22] G. Hong, P. Yang, H.-L. Huang, B. A. Baum, Y.-X. Hu, and S. Platnick, "The sensitivity of ice cloud optical and microphysical passive satellite retrievals to cloud geometric thickness," *IEEE Trans. Geosci. Remote Sens*., vol. 45, pp. 1315-1323, 2007.

[23] Y.-X. Hu, B. Wielicki, B. Lin, G. Gibson, S.-C. Tsay, K. Stamnes, and T. Wong, "Delta-fit: A fast and accurate treatment of particle scattering phase functions with weighted singular-value decomposition least-square fitting," *J. Quant. Spectrosc. Radiat. Transf.*, vol. 65, pp. 681-690, 2000.

[24] H.-L. Huang, P. Yang, H. Wei, B. A. Baum, Y.-X. Hu, P. Antonelli, and S. E. Ackerman, "Inference of ice cloud properties from high spectral resolution infrared observations," *IEEE Trans. Geosci. Remote Sens.*, vol. 42, pp. 842-853, 2004.

[25] D. P. Kratz, "The correlated *k*-distribution technique as applied to the AVHRR bands," *J. Quant. Spectrosc. Radiat. Transf.*, vol. 53, pp. 501-517, 1995.

[26] R. A. McClatchey, R. W. Fenn, J. E. A. Selby, F. E. Volz, and J. S. Garing, "Optical properties of the atmosphere," *Environ. Res. Pap., AFCRL-72-0497*, Air Force Cambridge Res. Lab., Bedford, MA, 1972.

[27] K. Meyer, P. Yang, and B.-C. Gao, "Optical thickness of tropical cirrus clouds derived from MODIS 0.66- and 1.375-μm channels," *IEEE Trans. Geosci. Remote Sens.*, vol. 42, pp. 833-841, 2004.

[28] P. Minnis, D. P. Garber, and D. F. Young, "Parameterizations of reflectance and effective emittance for satellite remote sensing of cloud properties," *J. Atmos. Sci.*, vol. 55, pp. 3313-3339, 1998.

[29] M. I. Mishchenko, W. B. Rossow, A. Macke, and A. A. Lacis, "Sensitivity of cirrus cloud albedo, bidirectional reflectance and optical thickness retrieval accuracy to ice particle shape," *J. Geophys. Res.*, vol. 101, pp. 16973-16985, 1996.

[30] D. L. Mitchell, "Parameterization of the Mie extinction and absorption coefficients for water clouds," *J. Atmos. Sci*., vol. 57, pp. 1311-1326, 2000.

[31] "MODIS Algorithm Theoretical Basis Document. MOD06," NASA, Greenbelt, MD, 1997.

[32] "MODIS Algorithm Theoretical Basis Document. MOD35," NASA, Greenbelt, MD, 1997.

[33] T. Nakajima and M. D. King, "Determination of the optical thickness and effective particle radius of clouds from reflected solar radiation measurements. Part I: Theory," *J. Atmos. Sci.*, vol. 47, pp. 1878-1893, 1990.

[34] S. L. Nasiri, B. A. Baum, A. J. Heymsfield, P. Yang, M. R. Poellot, D. P. Kratz, and Y.-X. Hu, "The development of midlatitude cirrus models for MODIS using FIRE-I, FIRE-II, and ARM in situ data," *J. Appl. Meteorol*., vol. 41, pp. 197-217, 2002.

[35] H. M. Nussenzveig, "Uniform approximation in scattering by spheres," *J. Phys*., vol. 21, pp. 81-109, 1988.

[36] S. Platnick, M. D. King, S. A. Ackerman, W. P. Menzel, B. A. Baum, J. C. Riédi, and R. A. Frey, "The MODIS cloud products: Algorithms and examples from Terra," *IEEE Trans. Geosci. Remote Sens.*, vol. 41, pp. 459-473, 2003.

[37] G. L. Potter and R. D. Cess, "Testing the impact of clouds on the radiation budgets of 19 atmospheric general circulation models," *J. Geophys. Res.*, vol. 109, pp. 2106-2115, 2004.

[38] F. Rabier, N. Fourrié, D. Chafaï, and P. Prunet, "Channel selection methods for Infrared Atmospheric Sounding Interferometer radiances," *Quart. J. Roy. Meteorol. Soc.*, vol. 128, pp. 1011-1027, 2002.

[39] G. Rädel, C. J. Stubenrauch, and R. Holz, "Retrieval of effective ice crystal size in the infrared: Sensitivity study and global measurements from TIROS-N Operational Vertical Sounder," *J. Geophys. Res*., vol. 108, pp. 4281-4293, 2003.

[40] W. L. Smith and C. M. Platt, "Comparison of satellite-deduced cloud heights with indications from radiosonde and ground-based laser measurements," *J. Appl. Meteor*., vol. 17, pp. 1796-1802, 1978.

[41] K. Stamnes, S.-C. Tsay, W. Wiscombe, and K. Jayaweera, "A numerically stable algorithm for discrete-ordinate-method radiative transfer in multiple scattering and emitting layered media," *Appl. Opt.*, vol. 27, pp. 2502-2509, 1988.

[42] J. L. Stith, J. E. Dye, A. Bansemer, A. J. Heymsfield, D. A. Grainger, W. A. Petersen and R. Cifelli, "Microphysical observations of tropical clouds," *J. Appl. Meteorol.*, vol. 41, pp. 97-117, 2002.

[43] C. J. Stubenrauch, R. Holz, A. Chedin, D. L. Mitchell, and A. J. Baran, "Retrieval of cirrus ice crystal sizes from 8.3 and 11.1 μm emissivities determined by the improved initialization inversion of TIROS-N operational vertical sounder observations," *J. Geophys. Res.*, vol. 104, pp. 793-808, 1999.

[44] Y. Takano, K.N. Liou, and P. Minnis, "The effects of small ice crystals on cirrus infrared radiative properties," *J. Atmos. Sci*., vol. 49, pp. 1487-1493, 1992.

[45] T. J. Uttal, A. Curry, M.G. McPhee, D. K. Perovich, R. E. Moritz, J.A. Maslanik, P. S. Guest, H. L. Stern, J. A. Moore, R. Turenne, A. Heiberg, M. C. Serreze, D. P. Wylie., P.O.G. Persson, C. A. Paulson, C. Halle, J. H. Morison, P. A.Wheeler, A. Makshtas, H. Welch, M. D. Shupe, J. M. Intrieri, K. Stamnes, R. W. Lindsey, R. Pinkel, W. S. Pegau, T. P. Stanton, and T. C. Grenfeld, "Surface heat budget of the Arctic Ocean, *Bull. Amer. Meteor. Soc*., vol. 83, pp. 255-275, 2002.

[46] S. G. Warren, "Optical constants of ice from the ultraviolet to the microwave," *Appl. Opt*., vol. 23, pp. 1206-1224, 1984.

[47] M. C. Webb, C. Senior, S. Bony, and J.-J. Morctrette, "Combining ERBE and ISCCP data to assess clouds in the Hadley Centre, ECMWF and LMD atmospheric climate models," *Clim. Dyn.*, vol. 17, pp. 905-922, 2001.

[48] H. Wei, P. Yang, J. Li, B. A. Baum, H.-L. Huang, S. Platnick, Y.-X. Hu, and L. Strow, "Retrieval of semitransparent ice cloud optical thickness from Atmospheric

Infrared Sounder (AIRS) measurements," *IEEE Trans. Geosci. Remote Sens.*, vol. 42, pp. 2254-2267, 2004.

[49] M. Wendisch, P. Pilewskie, J. Pommier, S. Howard, P. Yang, A. J. Heymsfield, C. G. Schmitt, D. Baumgardner, and B. Mayer, "Impact of cirrus crystal shape on solar spectral irradiance: A case study for subtropical cirrus," *J. Geophys. Res.*, vol. 110, pp. 3202-3219, 2005.

[50] B. A. Wielicki, R. D. Cess, M. D. King, D. A. Randall, and E. F. Harrison, "Mission to planet Earth: Role of clouds and radiation in climate," *Bull. Amer. Meteorol. Soc.*, vol. 76, pp. 2125-2153, 1995.

[51] W. Wiscombe, "Improved Mie scattering algorithms," *Appl. Opt.*, vol. 19, pp. 1505-1509, 1980.

[52] D. P. Wylie, W. P. Menzel, H. M. Woolf, and K. L. Strabala, "Four years of global cirrus cloud statistics using HIRS," *J. Clim.*, vol. 7, pp. 1972-1986, 1994.

[53] P. Yang, B. A. Baum, A. J. Heymsfield, Y.-X. Hu, H.-L. Huang, S.-C. Tsay, and S. Ackerman, "Single-scattering properties of droxtals," *J. Quant. Spectrosc. Radiat. Transfer*, vol. 79-80, pp. 1159-1180, 2003.

[54] P. Yang and K. N. Liou, "Finite-difference time domain method for light scattering by small ice crystals in three-dimensional space," *J. Opt. Soc. Amer. A*, vol. 13, pp. 2072-2085, 1996.

[55] P. Yang and K. N. Liou, "Geometric-optics-integral-equation method for light scattering by nonspherical ice crystals," *Appl. Opt.*, vol. 35, pp. 6568-6584, 1996.

[56] P. Yang, H. Wei, H. L. Huang, B. A. Baum, Y.-X. Hu, M. I. Mishchenko, and Q. Fu, "Scattering and absorption property database of various nonspherical ice particles in the infrared and far-infrared spectral region," *Appl. Opt*., vol. 44, pp. 5512-5523, 2005.

[57] P. Yang, K. N. Liou, K. Wyser, and D. Mitchell, "Parameterization of the scattering and absorption properties of individual ice crystals," *J. Geophys. Res*., vol. 105, pp. 4699-4718, 2000.

VITA

Biography

Kevin James Garrett was born in Wolfeboro, NH, where he lived permanently until graduating from Kingswood Regional High School in 1997. In Fall of that year, Kevin began is post-secondary education at Syracuse University before graduating in 2001 and entering a career in Information Technology. In May of 2004, Kevin then moved to Texas to pursue an education in Meteorology, and enrolled in graduate school at Texas A&M University in 2005. He may be contacted through the Department of Atmospheric Sciences, Texas A&M University, 3150 TAMU, College Station, TX, 77843.

Educational Background

Kevin received his B.S. in Information Management and Technology from Syracuse University, Syracuse, NY, in May 2001. He received his M.S. in Atmospheric Sciences from Texas A&M University, College Station, TX, in August 2007.